Research Article

Combined effects of waves and tides on bottom sediment resuspension in the southern Yellow Sea

Aimei Wang [a,b], Xiao Wu [a,b], Naishuang Bi [a,b], David K. Ralston [c], Chenghao Wang [d], Houjie Wang [a,b,*]

[a] College of Marine Geosciences, Key Laboratory of Submarine Geosciences and Prospecting Techniques, MOE, Ocean University of China, 238 Songling Rd., Qingdao 266100, China
[b] Laboratory of Marine Geology, Qingdao National Laboratory of Marine Science and Technology, No. 1 Wenhai Rd., Qingdao 266237, China
[c] Applied Ocean Physics and Engineering Department, Woods Hole Oceanographic Institution, Woods Hole, MA 02543, USA
[d] National Engineering Research Center of Port Hydraulic Construction Technology, Tianjin Research Institute for Water Transport Engineering, M.O.T., Tianjin 300456, China

ARTICLE INFO

ABSTRACT

A calibrated, coupled model (COAWST) of the Bohai and Yellow Seas was employed to examine the contributions of waves and tides to the sediment transport, and to understand the dynamic factors controlling bottom sediment resuspension around the Shandong Peninsula. The numerical results, which were consistent with the in-situ observations, illustrated two events with large values of suspended sediment concentration (SSC). The two events had similar wave heights, but SSC during the second event was more than twice that of the first one. Numerical experiments indicated that the large values of SSC east of the Shandong Peninsula were mainly ascribed to local resuspension, and that waves played a primary role in sediment resuspension for both high SSC events. The differences in SSC and bottom shear stress between the two events were mainly due to differences in wave period, representing about 65% of the total difference, and the non-linear interactions of wave and currents played a secondary role. Therefore, wave period is an important factor along with wave amplitude in the contribution of waves to sediment resuspension in this region. The combined actions of waves and currents dynamics dominate the sediment resuspension rather than either factor in isolation. Due to sheltering effect by the Shandong Peninsula, the wave effect on sediment resuspension was less to the south of the Peninsula than that to the north and east. In addition, the Shandong Coastal Current was enhanced by the northerly wind leading to more sediment transport southward along the coast of Shandong Peninsula, but this has small effect on the difference of suspended sediment concentration between two storm events.

1. Introduction

The coastal ocean plays an important role in global material cycling, acting as a sink by receiving terrestrial sediment, organic matters and other natural elements from rivers and as a source for the material delivered to the deep ocean (Martin et al., 1993; Holligan and Boois, 1993; Ramesh et al., 2015). Beside the terrestrial input from rivers, sediment resuspension by tides and waves affects sediment availability in coastal regions (Jiang et al., 2000, 2004; Wang et al., 2014b; Zeng et al., 2015; Luo et al., 2017). Sediment transport and accumulation in coastal regions are crucial to coastal sedimentation at various scales and to marine biogeochemical cycling and ecosystems through the

redistribution of particulate nutrients and pollutants (Schoellhamer, 1995; Brand et al., 2010; Dong et al., 2011). Understanding the driving forces for sediment resuspension, as well as potential interactions among the different factors affecting resuspension, is critical to interpreting the sediment transport in energetic coastal environments.

It has long been recognized that waves, currents and their nonlinear interactions are significant to resuspension and transport of sediment in coastal areas and the continental shelf (Sanford, 1994; Schoellhamer, 1995; Jing and Ridd, 1996; Jiang et al., 2000; Jiang et al., 2004; Shi et al., 2008; Brand et al., 2010; Miles et al., 2013; Bian et al., 2013a; Li et al., 2017; Fan et al., 2019). Previous studies have estimated that sediment mobilization is dominated by waves on about 80% of the

---
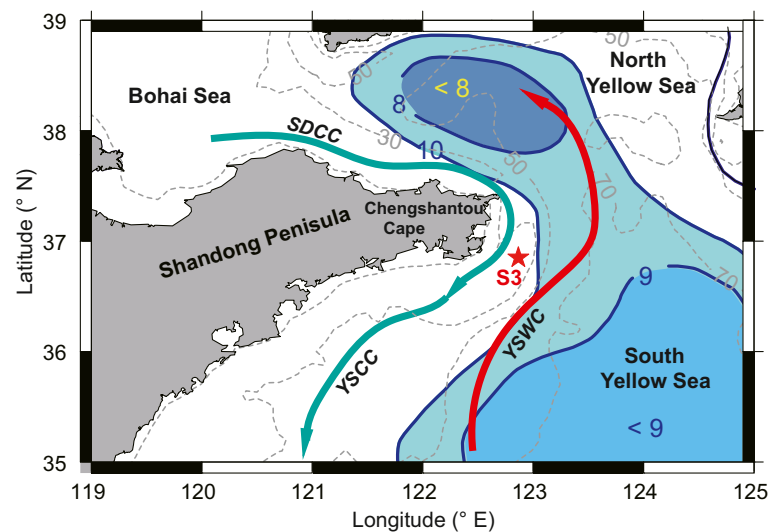
Fig. 1. Topography of the Bohai and Yellow Seas and circulation in winter: Yellow Sea Coastal Current in winter (YSCC), Yellow Sea Warm Current (YSWC), Shandong Coastal Current (SDCC). The red star indicates the location of mooring station S3, and the shaded area indicates the distribution of cold water mass. (For interpretation of the references to color in this figure legend, the reader is referred to the web version of this article.)

world's shelves, compared with 17% by tidal currents and 3% by ocean-current interactions (Walker, 1984; Swift et al., 1986). For example, Styles and Glenn (2005) found in observations off the coast of New Jersey that 63% of total sediment transport over a 2-year period was due to 32 winter storm events. Similarly, Miles et al. (2013) used glider-based observations to show that storm-driven sediment resuspension is an episodic process that dominates sediment transport on the Mid-Atlantic Bight. Numerical modeling has also highlighted the importance of waves for sediment resuspension in coastal regions such as the Bohai Sea, Yellow Sea and East China Seas (Yanagi and Inoue, 1995; Jiang et al., 2004; Bian et al., 2010; Zeng et al., 2015), Southern Californian shelf (Blaas et al., 2007), Adriatic Sea (Harris et al., 2008) and Hangzhou Bay (Shi et al., 2008). Li et al. (2017) presented that bed shear velocity was enhanced by storm-induced waves and currents by 5 times more than the normal conditions, and responsible for 3–4 orders of magnitude increase in sediment transport over the Grand Banks.

Waves are efficient in entraining significant amounts of sediment from the sea bed; however, there is almost no net sediment transport associated with the wave motion over a wave period, the length scale and direction of sediment transport are mainly controlled by the tidal currents and the wind-driven currents generated by the storm winds (Grant and Madsen, 1979; Harris et al., 2008; Warner et al., 2008; Guillou and Chapalain, 2011). The factors affecting the contribution of waves to sediment resuspension are various, including the wave amplitude, wave period, water depth (Schoellhamer, 1995; Jing and Ridd, 1996; Brand et al., 2010). For example, Schoellhamer (1995) estimated that bottom orbital velocity, which greatly influences the bottom shear stress, increased by 10% with a 10% increase in wave amplitude, 29% with a 10% increase in wave period, and 25% with a 10% decrease in water depth. Wang and Pinardi (2002) concluded that the longer-period waves generated by Sirocco winds were more capable of suspending sediment and created the potential for higher fluxes than waves associated with Bora winds in the northwestern Adriatic Sea. In regions with tides, variations in water depth can affect the strength of sediment resuspension by waves in resuspension. For example, in the South San Francisco Bay, seven out of nine wave-induced resuspension events were observed after low tides, indicating greater wave-induced sediment resuspension for shallower tidal depths (Brand et al., 2010). For locally generated waves, wind direction can affect the wind fetch and therefore alter wave amplitude (Schoellhamer, 1995). Remotely forced swell tends to have longer wave periods than local wind waves, potentially resulting in greater wave-induced bottom shear stress, as was

found for sediment resuspension in Cleveland Bay, North Australia (Jing and Ridd, 1996). Similarly, Fan et al. (2019) reported based on high-frequency acoustic observations that swell caused strong sediment resuspension in the Heini Bay, Yellow Sea.

The coast off the Shandong Peninsula, in the Yellow Sea is a region characterized by abundant sediment supply and strong waves and tidal dynamics, together with a prominent muddy deposit developed at high-stand sea level since the mid-Holocene (Milliman et al., 1987; Liu et al., 2002, 2004; Yang and Liu, 2007). Geophysical and geochemical evidences from various investigations consistently confirmed that this mud deposit was a distal sink of the Yellow River-derived sediment in the South Yellow Sea (Alexander et al., 1991; Bian et al., 2013a; Qiao et al., 2016; Xu et al., 2016). Both field observations and numerical modeling revealed high SSC around the cape of Shandong Peninsula in winter (Bian et al., 2013a, 2013b; Zeng et al., 2015; Zang et al., 2017; Wang et al., 2019), particularly during storm periods with large waves (e.g., Zhao et al., 2019). While it is acknowledged that waves contribute to the sediment resuspension in this region, the relative roles and interactions of waves and currents for sediment resuspension and transport remain poorly understood. For example, a mooring station east off the Chengshantou Cape recorded similar wave heights during two storm events with similar wind speed, however observed the bottom suspended sediment concentrations differing largely from each other (Zhao et al., 2019). It could not be reasonably interpreted by change of wave power. Here we used a calibrated model that coupled tide, wave and sediment modules in the Bohai and Yellow Seas, along with the observational data, to investigate the mechanisms of the sediment resuspension and transport in a highly energetic environment.

2. Regional setting

The Yellow Sea is a shallow and semi-enclosed marginal sea bordered by the mainland China and the Korean Peninsula, and it is connected with the Bohai Sea to the north and the East China Sea to the south (Fig. 1). The water depth of the Yellow Sea is 44 m in average, with a shallow region along the western coast, a NW-SE trough (Yellow Sea Trough) defined by the ~80 m isobath in the middle, and a steep, narrow shelf along the eastern coast.

Due to huge amounts of terrestrial sediment supply from the Yellow River (Huanghe) and the Yangtze River (Changjiang) and complex shelf circulation, several muddy depositional areas, known as "muddy patches", have developed to the northeast of Shandong Peninsula, in the
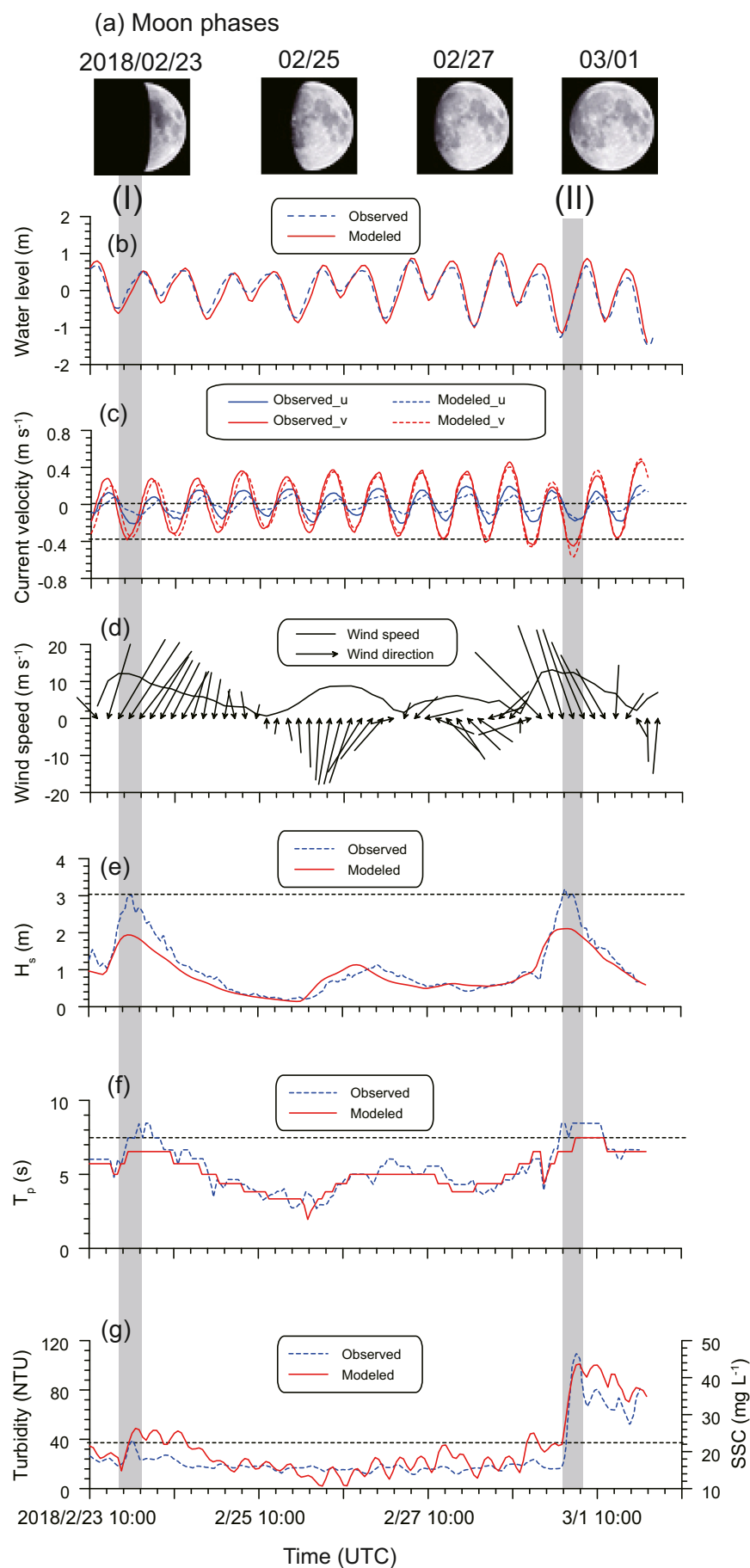
Fig. 2. Moon phases (a), and time series of water level (b), current velocity (c) (*u* for east-west component, *v* for north-south component), wind speed and wind vector at 10 m above the sea surface (d), significant wave height (H_s) (e), wave period (T_p) (f), bottom turbidity and suspended sediment concentration (SSC) (g) from observation and modeling at mooring station S3. The wind data was obtained from European Center for Medium-Range Weather Forecasts (ECMWF, http://www.ecmwf.int) with 3-h time resolution. The observed data collected at mooring station S3 were obtained from Zhao et al. (2019).

Table 1
Settings of numerical experiments.

	Control run	Experiment 1	Experiment 2	Experiment 3	Experiment 4
Tides	√	√	√	√	×
Winds	√	√	×	√*	√
Waves	√	×	×	√	√

1 * u component of wind direction was reversed but the velocity in Experiment 3 was the same to that of control run.

2 Symbols √ and × denote the experiments with and without the corresponding forces, respectively.

Yellow Sea trough, at the Old Yellow River Delta, southeast of the Yangtze Estuary and southwest of Cheju Island (Zhao et al., 1991; Saito and Yang, 1994; Liu et al., 2002, 2006, 2007, 2009; Li et al., 2005). A prominent mud deposit east off Shandong Peninsula is composed by fine-grained sediment (clayey-silty-sand and clayey silt) with median size of 5.5–6.5 Φ (~11–22 μm). Fine-grained sediment (silty clay) with median size <6 Φ (~16 μm) covers the other aforementioned muddy patches.

Tides in the Yellow Sea are mixed diurnal/semidiurnal (Naimie et al., 2001). M_2 is the dominant constituent, followed by S_2 and K_1 (Teague et al., 1998). The tidal range is greatest along the west coast of Korea (~3.5 m) and Chinese coast (~3.0 m) (Choi et al., 2003). The M_2 tidal currents along the western coast of Korea are about 60–80 cm s^{-1}, generally decrease to 20–40 cm s^{-1} along the east coast of China except for those near the Yangtze River Estuary, which are as high as 100 cm s^{-1} (Bao et al., 2001; Fang, 1986).

The modern circulation system in the Yellow Sea was established after the last high-stand sea level (Zong, 2004; Liu et al., 2010; Li et al., 2010, 2014) and it is strongly affected by the monsoonal climate. The winter circulation in the Yellow Sea is primarily composed by the Yellow Sea Coastal Current (YSCC) and the Yellow Sea Warm Current (YSWC). The former is a lower-temperature water mass that flows southward due to the northerly winds, whereas the latter carries warm and salty water northward along the western side of the Yellow Sea trough (Lie et al., 2009; Lin and Yang, 2011; Qu et al., 2018). The YSWC as a compensative current to the YSCC, is correspondingly enhanced in winter when the YSCC is strengthened by the northerly winds (Hsueh, 1988; Riedlinger and Jacobs, 2000; Teague and Jacobs, 2000). In summer, the Yellow Sea Cold Water Mass (YSCWM) is developed, with low temperature and high salinity, in the central Yellow Sea with stable thermocline (Li and Yuan, 1992; Park, 1986; Moon et al., 2009; Wang et al., 2014a; Xu et al., 2003; Zhang et al., 2008; Pang et al., 2004). Along the boundary of YSCWM, a cyclonic basin-scale current develops (Beardsley et al., 1992; Pang et al., 2004; Xia et al., 2006).

Wind waves play an important role in sediment distribution and transport patterns (Bi et al., 2011; Zang et al., 2017). Due to the dominance of the East Asian Monsoon, the southward-propagating waves with average significant wave heights of 0.9–1.9 m produced by the strong northerly winds are dominant in winter, whereas in summer the northward-propagating waves are weaker with significant wave heights of 0.5–1.0 m (Su and Yuan, 2005; Chen et al., 2016).

Due to variations in physical processes (e.g., wind, current, wave, hydrographic structure) (Choi et al., 2003; Chu et al., 1997; Naimie et al., 2001), the patterns of SSC, sediment transport and deposition in the Yellow Sea have strong seasonal and spatial variations. Studies have found greater sediment flux in winter than in summer, and large values of SSC have been identified to the east of the Shandong Peninsula, off the Old Yellow River Delta and outside the Yangtze River Estuary (Zang et al., 2017; Bian et al., 2013b; Lee and Chough, 1989; Luo et al., 2017; Wang et al., 2019). This study mainly focused on the sediment resuspension and transport process in winter in the vicinity of the Shandong Peninsula.

3. Methods

3.1. Model description

The model used in this study is the Coupled Ocean-Atmosphere-Wave-Sediment Transport (COAWST, Warner et al., 2008, 2010) Modeling System that combines several state-of-the-art modeling components, including the Regional Ocean Modeling System (ROMS, Shchepetkin and Mcwilliams, 2005) for ocean circulation, Simulating Waves Nearshore (SWAN, Booij et al., 1999) for waves, and the Community Sediment Transport Modeling System (CSTMS, Warner et al., 2008) for sediment transport. The models are coupled via the Modeling Coupling Toolkit (MCT, Jacob et al., 2005; Larson et al., 2005). ROMS and SWAN are two-way coupled, with SWAN sending wave information to ROMS including spectral wave heights, wavelengths, average wave periods at the surface and near the bottom, wave-propagation direction, near bottom orbital velocity, and wave energy dissipation rate. ROMS passes the water depth, sea-surface elevation, and current velocity to SWAN. In order to reduce the influence of open boundary conditions, the model domain covers the Bohai, the Yellow and the East China Seas. The model has a horizontal resolution of 1.5′ with 30 uniform layers in the vertical dimension. The atmospheric forcing data are interpolated from European Centre for Medium Range Weather Forecasts (ECMWF, http://www.ecmwf.int). Eight major tidal constituents (M_2, S_2, N_2, K_2, K_1, O_1, P_1, and Q_1) derived from the OSU TOPEX/Poseidon Global Inverse Solution (Egbert et al., 1994; Egbert and Erofeeva, 2002) are used as tidal forcing at the open boundary. HYCOM+NCODA Global 1/12 Analysis (GLBa0.08/expt_91.2) data are used to define sea-level, temperature, salinity and currents at the two open boundaries (south and east) and to create the initial conditions. The SWAN model uses the same horizontal grid and bathymetry as ROMS. The wave model is driven by the 3-h wind from ECMWF. Coupled model variables are exchanged between SWAN and ROMS every hour. In the sediment module, three particle classes are defined (clay, silt, and fine sand), and the initial condition for seabed composition is established using four characteristic bottom types composed of different fractions for the particle classes (sand, clayey silty sand, clayey silt, silty clay). More details of model set-up can be found in Wang et al. (2019). This simulation was run from February 1 to March 3, 2018, covering the time of field observations off the Shandong Peninsula.

Bed shear stress depended upon the relative magnitudes of the wave and current component as well as the bottom roughness, which were all related in a complex nonlinear fashion (Grant and Madsen, 1979). In this model, the bottom roughness is constant with $z_0 = 10^{-5}$ m. Wave-current BBL model (ssw_bbl) of Madsen (1994) was implemented to calculate the bottom shear stress. The wave-current-induced shear velocity (u_r) was calculated from formulas as follows:

$$u_r^2 = C_{mu}u_{wm}^2 = \left(u_{wm}^4 + 2u_c^2 u_{wm}^2 |cos\varnothing_{cw}| + u_c^4\right)^{\frac{1}{2}} \tag{1}$$

$$u_{wm}^2 = \tau_{wm}/\rho \tag{2}$$

$$C_{mu} = \left(1 + 2\mu|cos\varnothing_{cw}| + \mu^2\right)^{1/2} \tag{3}$$

$$\mu = \frac{\tau_c}{\tau_{wm}} = \left(\frac{u_c}{u_{wm}}\right)^2 \tag{4}$$

where u_{wm} is the shear velocity based on the maximum representative wave-associated shear stress, u_c is the current shear velocity, C_{mu} is a factor as controlled by μ and $\varnothing_{cw}$, while $\varnothing_{cw}$ expresses the angle between current direction and the direction of wave propagation, and μ is the ratio of current and wave bottom shear stress.

The wave-induced bottom shear stress (τ_{wm}) is related to the wave frictional coefficient (f_w) and wave orbital velocity (u_{br}).

$$\tau_{wm} = 0.5 f_w u_{br}^2 \tag{5}$$
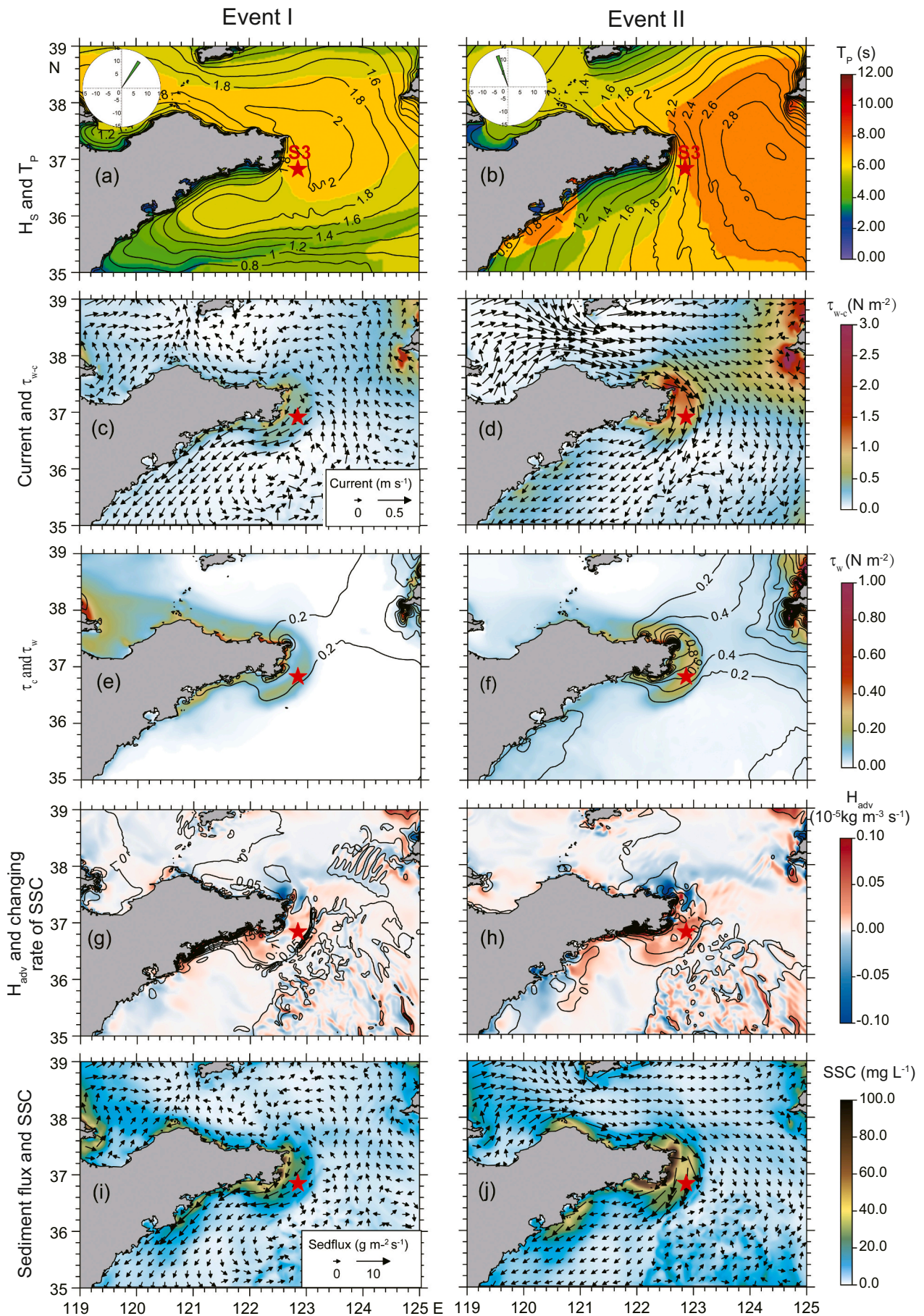
(caption on next page)

Fig. 3. Modeling results from the control run. Horizontal distribution of H_s (m, contour), T_p (s, color), and wind rose diagrams (upper left) (a, b), depth-averaged current (arrows) and wave-current-induced bottom shear stress (τ_{w-c}, color) (c, d), current-induced bottom shear stress (τ_c, N m^{-2}, contour) and wave-induced bottom shear stress (τ_w, color) (e, f), changing rate of near-bottom SSC ($\times 10^{-5}$ kg m^{-3} s^{-1}, contour) and bottom horizontal advection (H_{adv}, color)(g, h), and depth-averaged sediment flux (contour) and bottom SSC (color) (i, j) at 22:00, February 23 (Event I) and 3:00, March 1, 2018 (Event II) when the turbidity was highest at Station S3. (For interpretation of the references to color in this figure legend, the reader is referred to the web version of this article.)
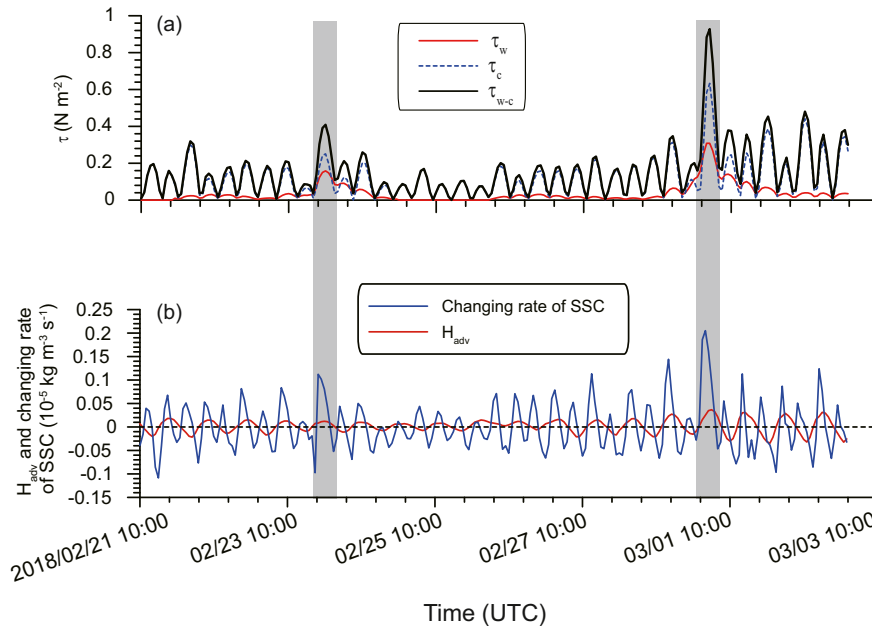
Fig. 4. Bottom shear stress induced by wave (τ_w), current (τ_c) and wave-current interaction (τ_{w-c}) (a), and the changing rate of near-bottom SSC and bottom horizontal advection (H_{adv}) (b) at the mooring station S3 from the control run.

According to Madsen (1994), f_w is calculated from:

$$f_w = \begin{cases} 0.43 C_{mu}, \dfrac{u_{br}}{k_N w_r} \leq 0.2 \\ C_{mu} exp\left(-8.82 + 7.02\left(\dfrac{u_{br}}{K_N w_r}\right)^{-0.078}\right), 0.2 < \dfrac{u_{br}}{k_N w_r} \leq 100 \\ C_{mu} exp\left(-7.30 + 5.61\left(\dfrac{u_{br}}{K_N w_r}\right)^{-0.109}\right), 10^2 < \dfrac{u_{br}}{k_N w_r} \leq 10^4 \\ C_{mu} exp\left(-7.30 + 5.61(10000)^{-0.109}\right), \dfrac{u_{br}}{k_N w_r} > 10^4 \end{cases} \tag{6}$$

where w_r represents wave radian frequency and k_N is the Nikuradse roughness.

The current-induced bottom shear stress (τ_c) is obtained from:

$$\frac{1}{\rho}\tau_c = u_c^2 \tag{7}$$

$$u_c = \frac{u_r}{2}\frac{ln(z_r/\delta_{wc})}{ln(\delta_{wc}/z_0)}\left(-1+\sqrt{1+\frac{4kln(\delta_{wc}/z_0)}{(ln(z_r/\delta_{wc}))^2}\frac{u_{cr}}{u_r}}\right) \tag{8}$$

k is von Karman's constant ($k = 0.4$), u_{cr} is current velocity, z_r is a reference elevation, z_0 is roughness lengths. δ_{wc} is the wave boundary layer thickness, which can be obtained from:

$$\delta_{wc} = \begin{cases} \dfrac{2ku_r}{\omega_r}, & C_{mu}\dfrac{u_{br}}{k_N w_r} > 8 \\ k_N, & C_{mu}\dfrac{u_{br}}{k_N w_r} \leq 8 \end{cases} \tag{9}$$

3.2. Model performance

The model used here has been validated for tides, water level, currents, waves, temperature and SSC with the coefficient of determination (R^2), the root-mean-square error (RMSE), and the skill score (SS) in a previous study that investigated the sediment transport and deposition by a seasonal thermal front at the eastern tip of Shandong Peninsula (Wang et al., 2019). Here, the model performance was further evaluated using time-series datasets including water level, bottom current
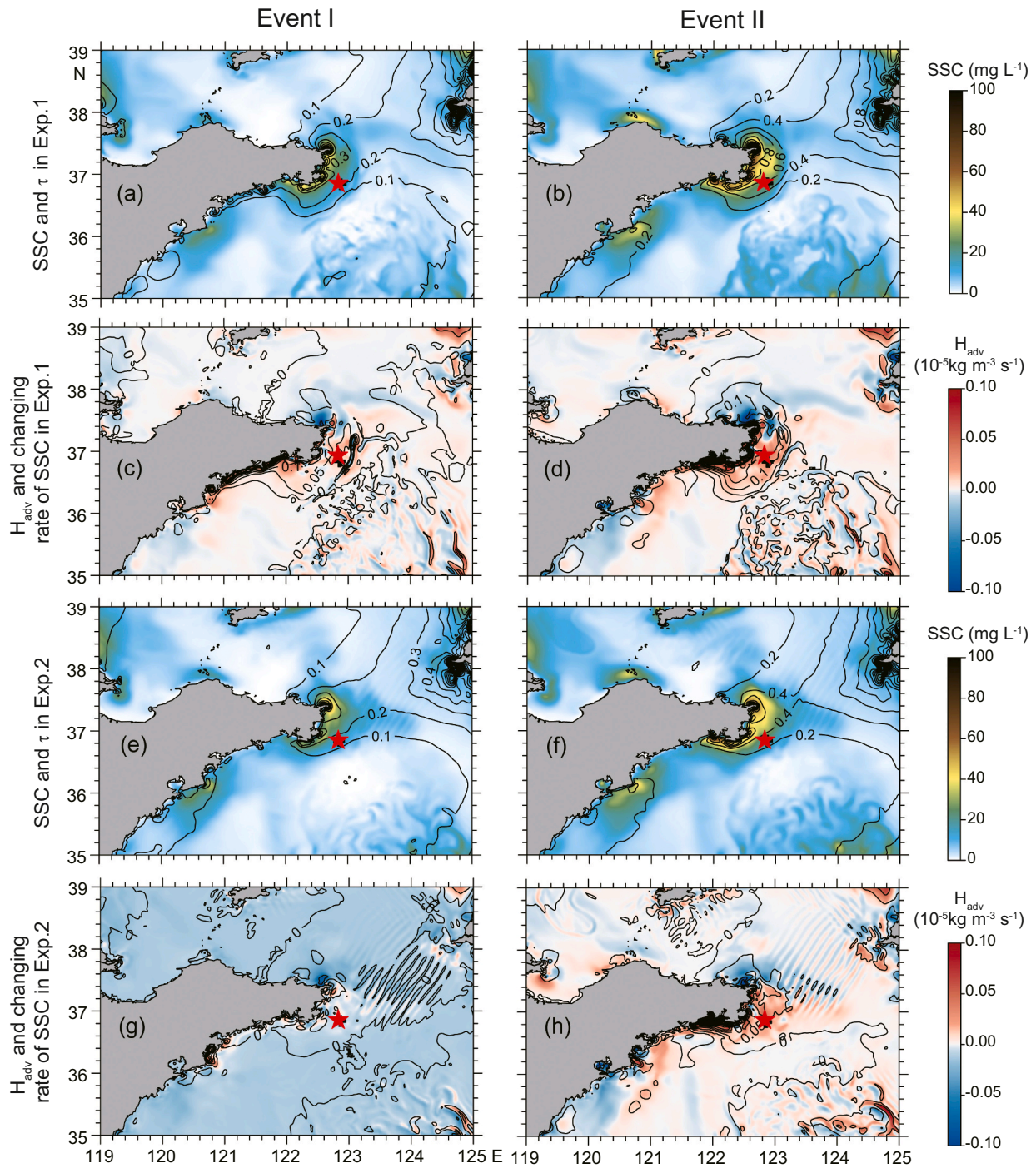
Fig. 5. Numerical results from Experiment 1 (no waves) and Experiment 2 (no wind, no waves). Horizontal distribution of bottom shear stress (τ, N m^{-2}, contour) and bottom SSC (color) (a, b), changing rate of near-bottom SSC ($\times 10^{-5}$ kg m^{-3} s^{-1}, contour) and bottom horizontal advection (H_{adv}, color) (c, d), at Event I and Event II from Experiment 1. Horizontal distribution of bottom shear stress (τ, N m^{-2}, contour) and bottom SSC (color) (e, f), changing rate of near-bottom SSC ($\times 10^{-5}$ kg m^{-3} s^{-1}, contour) and bottom horizontal advection (H_{adv}, color) (g, h), at Event I and Event II from Experiment 2. (For interpretation of the references to color in this figure legend, the reader is referred to the web version of this article.)
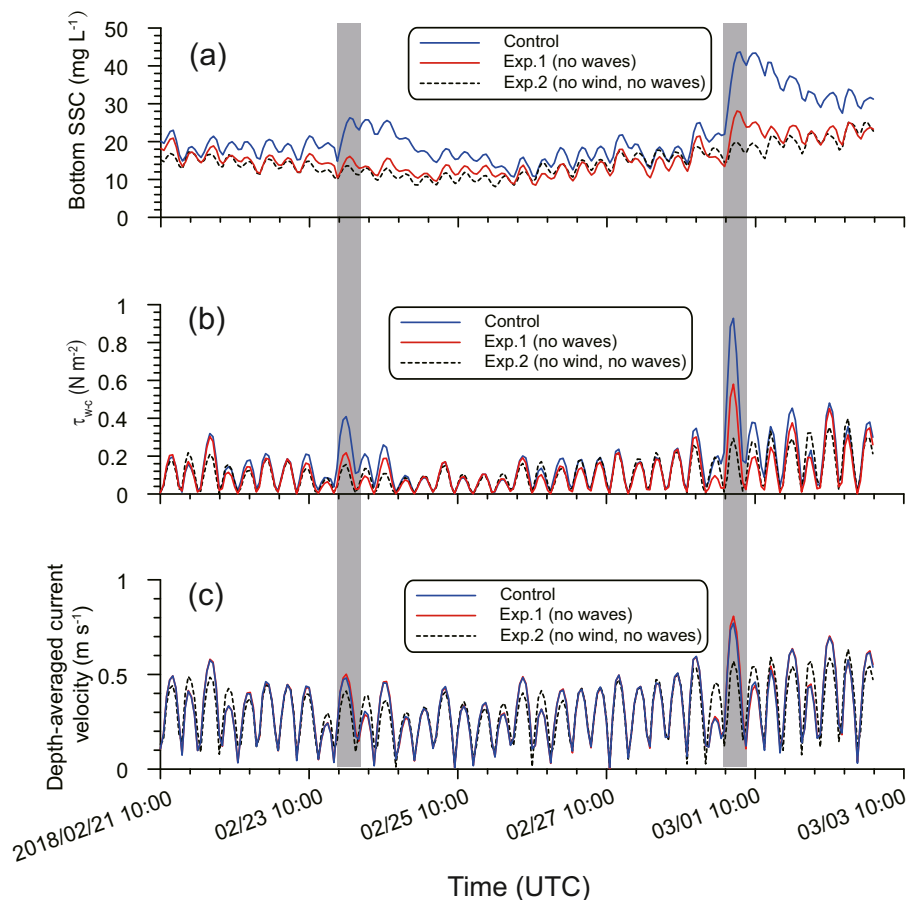
Fig. 6. Comparison of numerical results from the Control run, Experiment 1 (no waves) and Experiment 2 (no wind, no waves): bottom SSC (a), wave-current-induced bottom shear stress (τ_{w-c}) (b) and depth averaged current velocity (c)) at station S3.

velocity, significant wave heights, wave period and the bottom SSC that were collected by a mooring system deployed at station S3 in February–March 2018 (Zhao et al., 2019; Fig. 1). The mooring station S3 was located at the east tip of Shandong Peninsula (36.86°N, 122.87° E), with an average water depth of ~27 m (Fig. 1). The mooring observations were collected from February 23 to March 2, 2018. A tripod deployed at the seabed was equipped with a Nortek 6 MHz ADV, a RDI WorkHorse 600 kHz ADCP and a RBR Turbidity Meter (RBR-Tu). Near-bottom velocity (with eastward, northward and vertical components denoted by u, v, and w) were recorded by the downward-looking ADV, mounted at 0.71 m above the bottom. The ADV measurements were taken in burst mode with a sampling frequency of 32 Hz. Each burst lasted for 10 min with a bursting interval of 1 h. The RBR-Tu was positioned at 1.16 m above the bottom and was operated in a continuous mode to collect near-bottom turbidity every 10 s. The significant wave heights, wave period and water depth were measured every 20 min by the upward-looking ADCP.

Comparisons indicate that model results generally agree with the observations at station S3. Quantitative skill assessments presented a determination coefficient (R^2) of 0.90 for water level, and slightly lower values for bottom current speed ($R^2 = 0.87$). The wave model was run using default input parameters. The model reproduced the time series of waves with significant wave heights during two storm events that were 30% less than the observations (Fig. 2), and the maximum wave period was about 1–2 s less than in the observations. The lower wave amplitude in the model may be due to the uncertainty in the model bathymetry and an underestimate of the wind speed used to force the wave model (Komen et al., 1994). Moreover, the ECMWF model results that are used

to force the wave model may underrepresent the wind magnitude, as has been found in coastal regions including the Bohai Sea (Lv et al., 2014), the Adriatic Sea (Signell et al., 2005), the Agulhas Current region (Nkwinkwa et al., 2019).

The modeled time series of bottom SSC were generally consistent with the observed turbidity. Both the observed turbidity and the modeled SSC increased significantly during the two storm events together with increasing significant wave heights, with two-fold increases of both SSC and turbidity during the second event (Fig. 2). The model generally captured the dominant features of the currents, wave conditions, and the corresponding SSC variations, which provides a basis for investigating the sediment resuspension and transport processes.

To examine the mechanisms of sediment transport and to interpret the differences in SSC over the two storm events, five numerical experiments were conducted (Table 1). The control run included all the driving forces (winds, waves and tides). Experiment 1 eliminated the waves but kept the other forces (tides and winds) to test the wave effect on the sediment resuspension. In Experiment 2, waves and wind were eliminated and only tides were taken into account to compare with results in the control run and Experiment 1 to test the contribution of winds and waves to sediment resuspension. In Experiment 3, all the forcing factors (winds, waves and tides) were considered, but the east-west wind direction was reversed and the north-south wind direction was kept as the control run in order to test the wind direction effect on the discrepancy of SSC between the two storm events. Experiment 4 eliminated the tides but kept the other forcing factors (winds and waves) to test the contribution of waves to the discrepancy of SSC between the
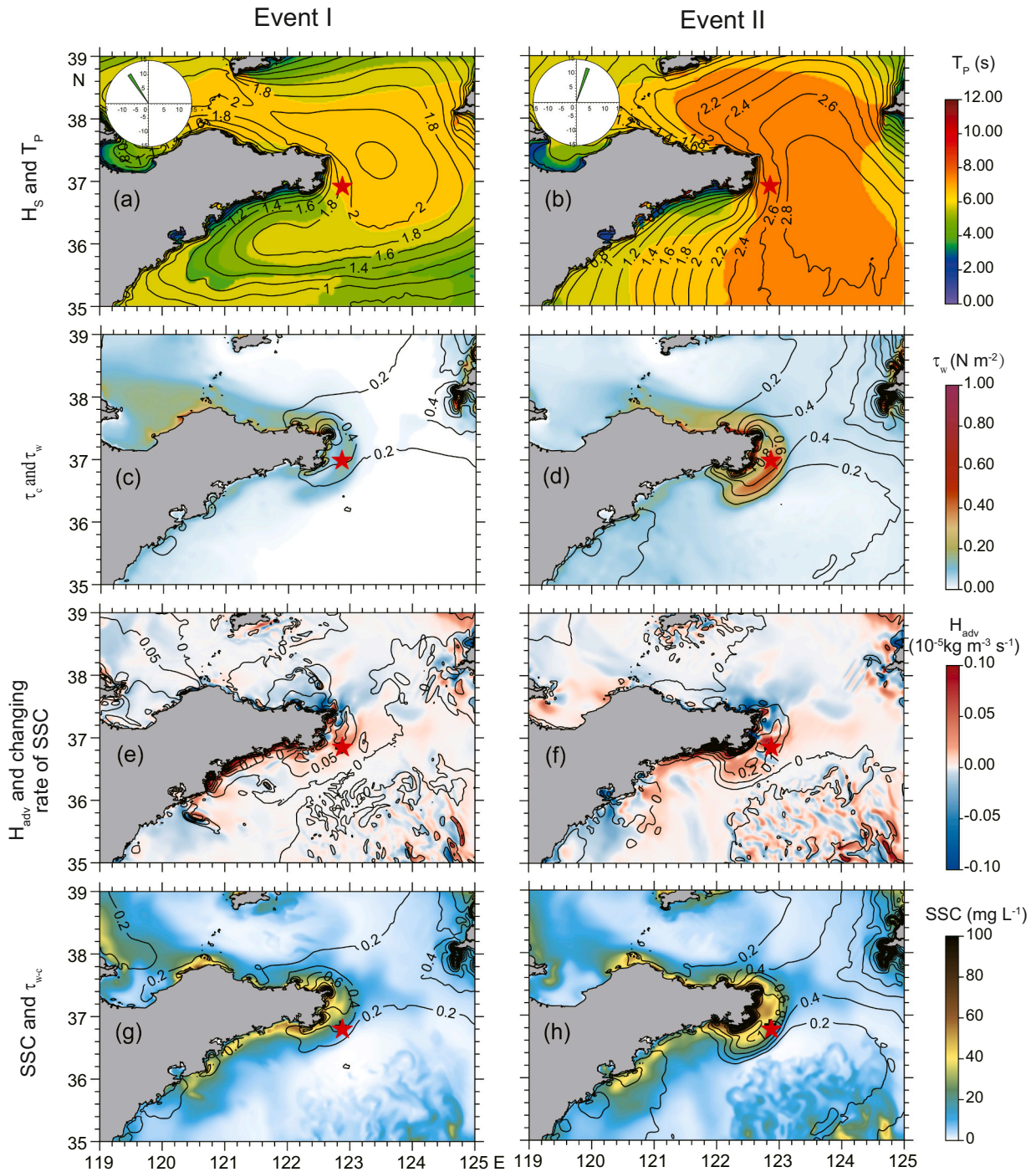
Fig. 7. Numerical results from Experiment 3 (reversed wind direction). Horizontal distributions of significant wave height (H_s, m, contour), wave period (T_p, s, color), and wind rose diagrams (upper left) (a, b), current-induced bottom shear stress (τ_c, N m^{-2}, contour) and wave-induced bottom shear stress (τ_w, color) (e, f), changing rate of near-bottom SSC ($\times 10^{-5}$ kg m^{-3} s^{-1}, contour) and bottom horizontal advection (H_{adv}, color)(g, h), and wave-current-induced bottom shear stress (τ_{w-c}, N m^{-2}, contour) and bottom SSC (color) (i, j) at 22:00, February 23 (Event I) and 3:00, March 1, 2018 (Event II), respectively. (For interpretation of the references to color in this figure legend, the reader is referred to the web version of this article.)
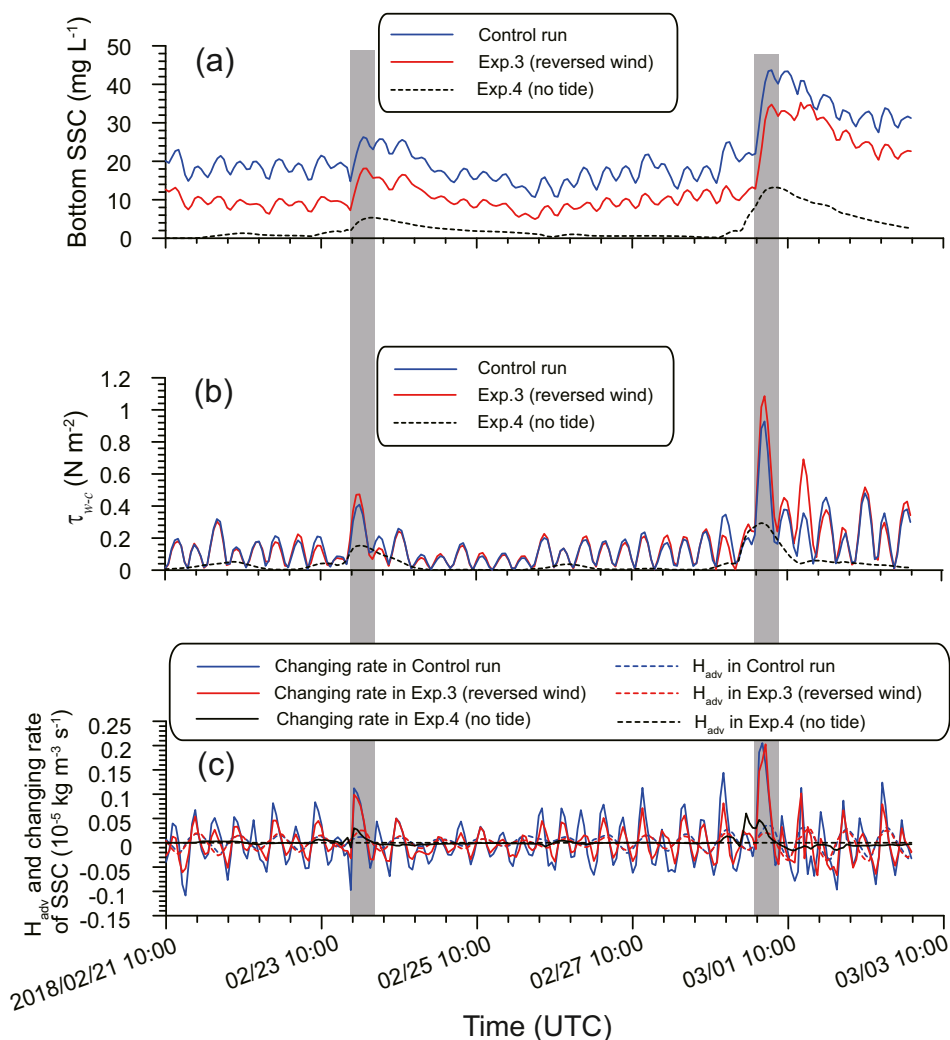
Fig. 8. Comparison of numerical results from the control run, Experiment 3 (reversed wind direction) and Experiment 4 (no tide): bottom SSC (a), wave-current-induced bottom shear stress (τ_{w-c}) (b), changing rate of near-bottom SSC and bottom horizontal advection (H_{adv}) (c) at station S3.

two storm events. The diagnostic momentum terms like the changing rate with time and horizontal advection of SSC were derived directly from the numerical results. The momentum equations can be found in Warner et al. (2008).

4. Results

4.1. Sediment resuspension and transport patterns due to winds, waves, and tides

The two storm events with significant bursts of both observed turbidity and modeled SSC in bottom layer are marked as event I and event II (Fig. 2g). The turbidity of event II (peak turbidity of 109 NTU) was more than twice that of the event I (peak turbidity of 40 NTU), even though they were under similar waves conditions. The turbidity of the event II also decreased more slowly than the event I. For both events, the SSC increase started at the beginning of flood tide when the water level was the lowest. The observations spanned a neap-to-spring tidal cycle from February 23 to March 2, 2018, with event I during neap tides on February 24 and event II during spring tides on March 1 (Fig. 2a). While the difference in current between the two events was <0.1 m s^{-1} (Fig. 2c), the tidal range increased from 0.5 m at neap tide to 1.9 m at spring tide (Fig. 2a, b). Wind data obtained from European Center for

Medium-Range Weather Forecasts (ECMWF, http://www.ecmwf.int) with 3-h resolution indicated that the peak wind speeds during those two events were similar to each other. As a result, the peak significant wave heights were similar (Fig. 2e, f) with 3.0 m and 3.2 m during those two events, respectively. Wave periods were slightly greater during the second event when turbidity was largest, with peak periods of about 7.6 s and 8.5 s in events I and II, respectively. The wind directions during the two storm events were different, with northeasterly winds prevailing in event I and northwesterly winds in event II.

Model results illustrate the horizontal distribution of sediment and hydrodynamics features at 22:00, February 23 and 3:00, March 1, 2018 when the turbidity was the highest in the control run (Fig. 3). In both events, strong northerly winds intensified the waves-induced bottom shear stress east of the Shandong Peninsula, which lead to rapid increases in near-bottom SSC (Fig. 3g, h) and large values of near-bottom SSC (Fig. 3i, j). The SSC and its changing rate of near-bottom SSC decreased offshore along with the decrease in bottom shear stress (Fig. 3). Similar to the bottom shear stress induced by the nonlinear wave-current interactions, wave-induced bottom shear stress and current-induced bottom shear evidently increased at the east of Shandong Peninsula and decreased offshore (Fig. 3e, f). The northwesterly winds during event II reinforced the coastal current around the Shandong Peninsula and enhanced the southward sediment transport. In
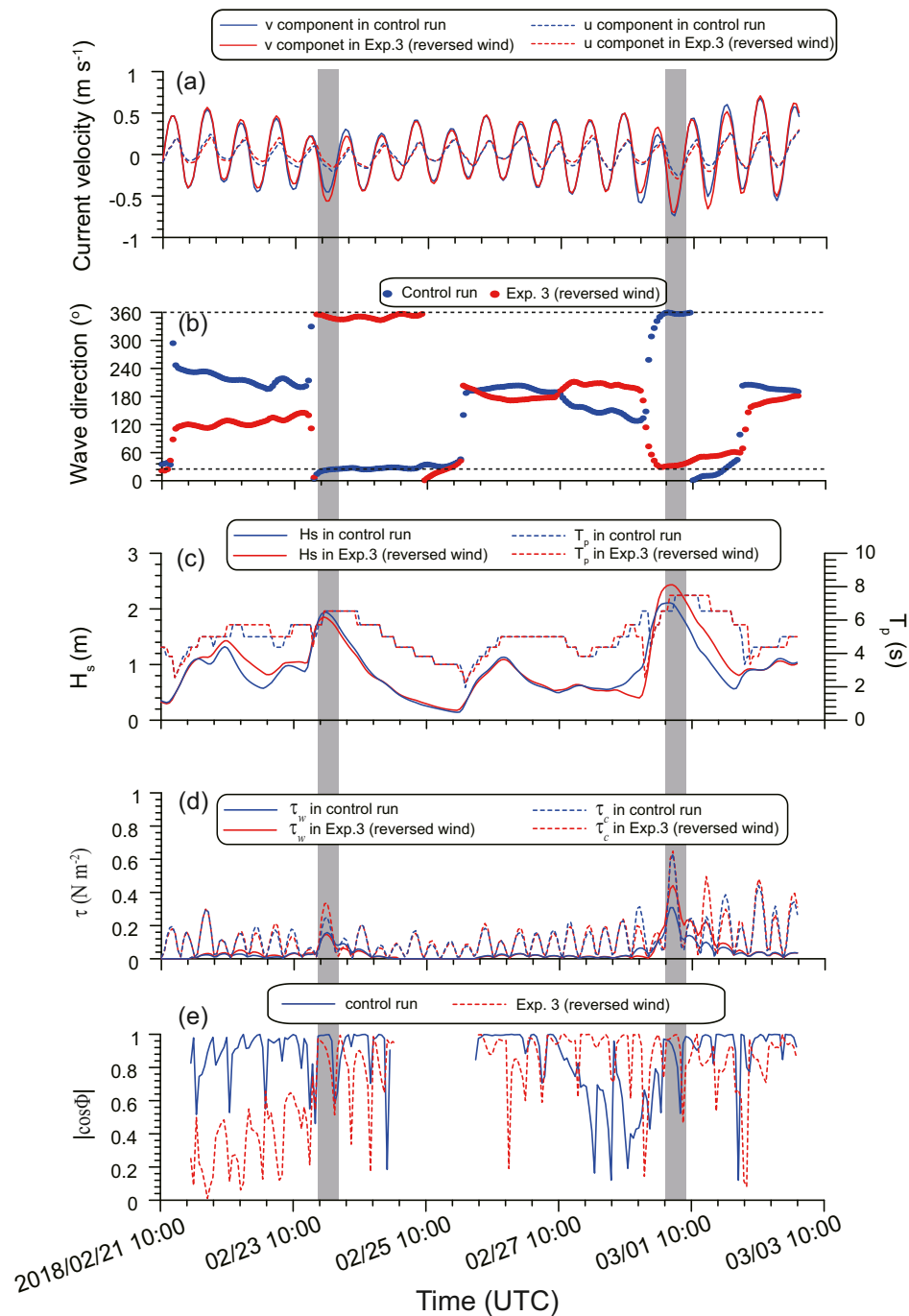
Fig. 9. Comparison of current (a), wave direction (b), significant wave height (H_s) and wave period (T_p) (c), bottom shear stresses (τ) (d), and parameter $|cos\phi|$ (e) from the Control run and Experiment 3 (reversed wind direction) at station S3.

contrast, the northeasterly winds during event I forced the coastal current flowing westward on the northern side of Shandong Peninsula and southward on the southern side, producing an evident divergence of sediment transport around the Chengshantou Cape (Fig. 3c, d, i, j).

It was notable that the SSC during the event II was about twice that during the event I (Fig. 3i, j). High SSC generally represents the contributions by both horizontal advection by currents and stress-induced local resuspension (Yu et al., 2012; Xiong et al., 2017). To diagnose the contribution of horizontal advection and local resuspension to the SSC change, the changing rate of near-bottom SSC with time and the bottom horizontal advection term at station S3 were analyzed based on

the numerical results from control run (Fig. 4b). The bursts of bottom SSC during the two storm events well corresponded with increase in bottom shear stress induced by wave-current interactions (Fig. 4), whereas the horizontal advection of SSC seemed to be varying periodically with the tidal oscillations, one order in magnitude lower than the changing rate of SSC with time particularly during the storm events (Fig. 4b). Therefore, the active sediment resuspension by wave-current interactions was primarily dominant over the significant increases in near-bottom SSC during storm events.
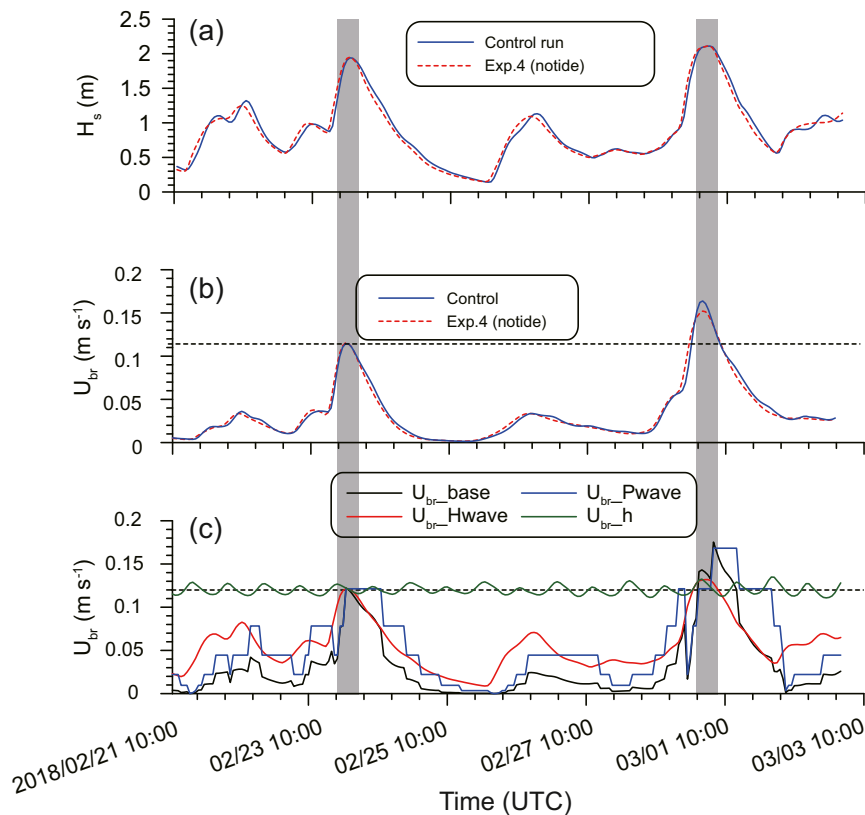
Fig. 10. Comparison of significant wave height (H_s) (a), wave-induced bottom orbital velocity (U_{br}) (b) from the Control run and Experiment 4 (no tide) at station S3, and wave-induced bottom orbital velocity calculated from the JONSWAP spectrum (Wiberg and Sherwood, 2008) (c, U_{br_base} was the base case with all varying parameters output from the control run, U_{br_Hwave} means wave height was variable while wave peak period and water depth were kept constant (T_p = 6.54 s, h = 24 m), U_{br_Pwave} means wave peak period was variable while wave height and water depth were kept constant (H_s = 1.94 m, h = 24 m). U_{br_h} means water depth was variable while wave height and wave peak period were kept constant (H_s = 1.94, T_p = 6.54 s).

4.2. Differences in SSC between the two storm events

Bottom shear stresses greatly enhanced sediment resuspension during the two events, but the bottom turbidity during event II was more than twice that during event I even though the two storm events had similar wave heights. Thus, we examine the contributions of wave and current to the differences in bed shear stress and SSC between the two events.

Bottom shear stress evidently increased during the storm events along with increasing wave heights and enhanced currents, much higher than those during calm weather (Figs. 3 and 4). The wave-current-induced bottom shear stress during event II was found to be more than twice of that during event I (Fig. 3). However, when the effects of waves were removed in Experiment 1 and waves and wind were both removed in Experiment 2, the resultant bottom shear stress and near-bottom SSC decreased significantly (Figs. 5 and 6). In Experiment 1 the deactivation of wave model decreased the bottom shear stress by 20–30% compared with the control run, resulting in ~40% of decreases in bottom SSC during the storm events. However, the presence of storm winds evidently enhanced the bottom shear stress as the N-S component of current velocity was enhanced. When the tides became the only driving force, the bursts of bottom SSC and shear stress disappeared during the time of storm events. It seemed that the wind and waves should play a dominant role in the local sediment resuspension.

Given the similar wind speeds during the two storm events, the difference in wind direction might be responsible for different responses of wave-current interactions and sediment resuspension to the storms. To identify the contribution of wind direction to the differences in SSC between the two events, wind directions during the two events were altered with wind speeds unchanged in Experiment 3 as the northeasterly wind during event I was switched to be northwesterly, and the northwesterly wind during event II was changed to be northeasterly. The numerical results from Experiment 3 indicate that the wind reversal produced overall similar horizontal distribution pattern of bottom SSC with larger values at east tip of Shandong Peninsula and decreasing offshore as in the control run (Fig. 7). The bottom SSC decreased in Experiment 3, whereas the changing rate of bottom SSC with time was comparable to the results of control run (Figs. 7 and 8). The similar changing rates of bottom SSC between Experiment 3 and the control run were possibly ascribed to the joint effect of bottom sediment resuspension and horizontal advection. Wave propagation direction changes with the wind direction, whereas the wave periods and $|cos\varnothing_{cw}|$ (in Eq. (3)) were similar at station S3 during the two events between two experiments (Figs. 7a, b and 9). Thus, the small changes in wind direction had little effect on wave period variation. The discrepancy of wave periods between the two storm events might be ascribed to the waves propagation from other areas, such as the Bohai Sea, where wind fields were largely different from each other; nevertheless the wind speeds and direction recorded at station S3 were almost unchanged. The numerical results from Experiment 3 indicated that increase of H_s under north-easterly winds led to slightly greater wave-induced and wave-current-induced bottom shear stress, which resulted in more sediment resuspension (Fig. 8). However, northwesterly winds were conducive to sediment transport by strengthening the non-tidal currents and led to a slight increase of sediment horizontal advection (Figs. 7, 8). Overall, the SSC difference between those two storm events and the changing rate of near-bottom SSC with time during the two events presented similarity to those from the control run (Fig. 8c). That suggested the reversal of wind direction should not be the primary factor that induced the large discrepancy of bottom SSC between the two storm events without wave period change.

To examine contributions of the wave component to the differences in SSC between the two storm events, Experiment 4 was set without considering tidal current. In Experiment 4, there was almost no sediment horizontal advection, whereas the two burst of sediment resuspension still appeared (Fig. 8a). Due to the lower bottom shear stress without the
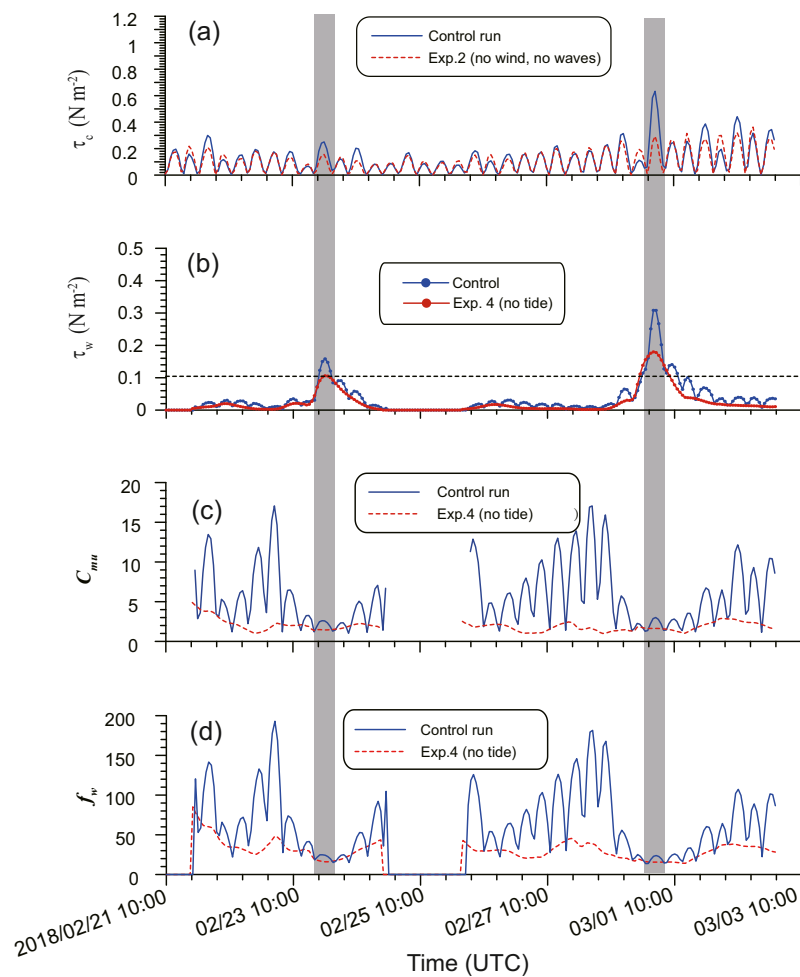
Fig. 11. Comparison of current-induced bottom shear stress (τ_c) from the Control run and Experiment 2 (no wind, no waves) (a), and comparison of wave-induced bottom shear stress (τ_w) (b), C_{mu} (c) and f_w (d) from the Control run and Experiment 4 at station S3.

tidal currents (Fig. 8b), the bottom SSC (Fig. 8a) and changing rate of near-bottom SSC (Fig. 8c) were much less than those in the control run. Removal of tidal forcing also reduced the difference in bottom SSC between the two events (Fig. 8a). Model results shown that the maximum wave-induced bottom shear stress of event II increased 65% (Fig. 11b) than that of event I due to 30% increase of near-bottom wave orbital velocity (Fig. 10a) in Experiment 4. The near-bottom wave orbital velocity was calculated using JONSWAP spectrum based on the model-output parameters including significant wave height (H_s), peak period (T_p) and water depth (h) (Wiberg and Sherwood, 2008), which presented similar distribution patterns to the model results (Fig. 10c). The near-bottom wave orbital velocity of event II increased to >30% than that of event I with all varying parameters output from the control run. To examine the individual contributions of the significant wave height, peak period and water depth to wave orbital velocity, a group of tests were conducted. When the water depth varied with tides, and the significant wave height and peak period were kept constant ($H_s = 1.94\ m$, $T_p = 6.54\ s$), the wave orbital velocity varied around $0.12\ \mathrm{m\ s^{-1}}$ with the water depth. Thus, the variation of water level has little effect on the wave orbital velocity and wave-induced bottom shear stress. When the wave period was kept constant ($h = 24\ m$, $T_p = 6.54\ s$), the wave orbital velocity varied with H_s, as slight difference between the two storm events was identified. When the water depth and the wave height were kept constant ($h = 24\ m$, $H_s = 1.94\ m$), the wave orbital velocity varying with the wave peak period (T_p) presented evident discrepancy between

the two storm events. As a result, the 65% difference of maximum wave-induced bottom shear stress between the two events was mainly ascribed to the variation of wave period.

To examine the contributions of the nonlinear wave-current interactions to the differences in SSC between the two storm events, model results from Experiment 2 (no wind, no waves) and Experiment 4 (without considering tidal current) were compared with the control run. As aforementioned, the significant increases of SSC at east of Shandong Peninsula were dominantly ascribed to local sediment resuspension induced by bottom shear stress. Thus, only the contribution of nonlinear wave-current interactions to the bottom shear stress was considered here. Comparison of the current-induced bottom shear stress between the control run and the Experiment 2 indicated that current-induced bottom shear stress has been greatly enhanced by the waves (Fig. 11a). Correspondingly, the wave-induced bottom shear stress was enhanced by the current, though the significant wave height and wave-induced bottom orbital velocity were similar between the Experiment 4 and control run (Fig. 10). That increase is ascribed to the wave-current interaction by the factor C_{mu} (Eq. (1)), which is controlled by the ratio of current and wave bottom shear stress (μ) and the angle between current direction and the direction of wave propagation ($\varnothing_{cw}$) (Eq. (3)). The factor C_{mu} is about 17% larger in event II than that in event I, resulting in higher wave-induced shear stresses during event II, as well as the discrepancy in SSC between the two events at station S3 (Fig. 11c). Comparison of results from Experiment 4 and the control run indicated
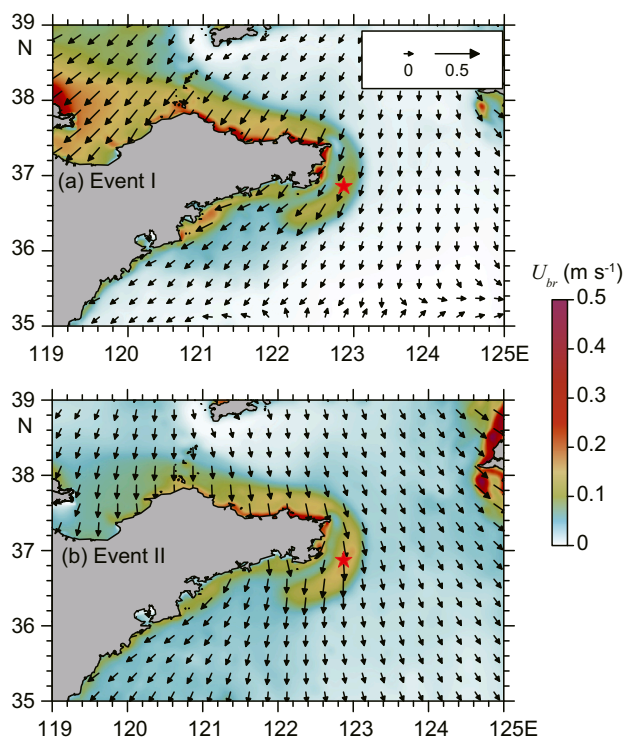
Fig. 12. Horizontal distributions of near-bottom wave orbital velocity (U_{br}) at 22:00, February 23 (a) and 3:00, March 1 (b) in the Control run when the turbidity was the highest at Station S3.

the wave frictional coefficient (f_w) has been increased with the presence of tidal current leading to larger wave-induced bottom shear stress (Fig. 11d, Eq. (5)). However, comparison of two high storm events in the control run, the wave frictional coefficient (f_w) was similar. Thus, the contributions of the current to the wave-induced bottom shear stress were similar between the two events (Eqs. (5) and (6)). The non-linear interactions between waves and currents contributed to the evident difference between those two events at location S3 by the increased factor C_{mu}.

Therefore, despite of similar wave heights during the two storm events, the waves with longer period in event II produced higher wave orbital velocity and associated higher bottom shear stress than during event I, which eventually explained 65% of the difference of bottom SSC between the two events. The nonlinear wave-current interactions played a secondary role in producing the abnormal highs of SSC during event II.

5. Discussion

East Asian Monsoon plays an important role in sediment resuspension in a shallow marginal sea with distinct spatial variability. In winter, the prevailing strong northerly winds led to large wave height in the Yellow Sea (Fig. 3a, b). Due to the sheltering effect of the Shandong Peninsula, the wave-induced bottom orbital velocity was larger at the north and east sides of the Shandong Peninsula, whereas it became smaller to the south (Fig. 12). In combination with large current-induced bottom shear stress, bottom shear stress induced by wave and current was high at the east tip of Shandong Peninsula (Fig. 3). As a result, high SSC induced by local resuspension was found around the east tip of Shandong Peninsula (Fig. 3) and it decreased seaward, which was consistent with the monthly distribution patterns from the previous works (Bian et al., 2013a, 2013b; Zeng et al., 2015; Zang et al., 2017; Wang et al., 2019).

The circulation pattern in the Yellow Sea was also strongly affected

by the winds in winter. Under the circumstance of strong northerly winds, the coastal current was enhanced as it flowed southward, especially during event II. The surface residual current can reach >30 cm s^{-1} in the north-south component at station S3 (Figs. 3 and 13). During the northerly wind relaxations or reversals, the coastal current flowed northward, which were consistent with recent investigations (Yuan et al., 2008; Hu et al., 2017; Ding et al., 2019; Wu et al., 2019; Wang et al., 2020). In winter, when strong northerly winds prevailed, intensified coastal current and strong resuspension led to a large amount of suspended sediment being transported southward from the east of Shandong Peninsula (Figs. 2 and 13) and more sediment was transported southward during event II. Nevertheless, high sediment flux was confined within a very limited area around the east tip of Shandong Peninsula, rather than a long belt with high-concentrated sediment wrapping the whole Shandong Peninsula from the Bohai Sea to the Yellow Sea. This result implied that the high SSC at the east tip of Shandong Peninsula was primarily ascribed to local resuspension under stormy conditions, rather than the horizontal advection from the Yellow River.

Recent studies also illustrated that the modern sediment accumulation rate was low east of the Shandong Peninsula (Fig. 14a, Zhao et al., 1991; Li et al., 2002; Zhang et al., 2009; Hu et al., 2011). The vertical distributions of radioisotope ^{210}Pb at sediment cores HS-4, YZ-21 and KC-10 (locations were shown in Fig. 15) showed strong vertical mixing with a uniform distribution of total ^{210}Pb from surface to bottom, which implied there might be less sediment accumulation over the past 100 years (Li et al., 2002; Zhang et al., 2009; Hu et al., 2011). The grain-size distribution of surface sediment indicated coarser surface sediment at the seabed around the east tip of Shandong Peninsula (Fig. 14b), possibly related to the decreasing supply of Yellow River-derived sediment (Wang et al., 2017) and the physical sorting by strong wave-current interactions. Therefore, the mud deposit at east tip of Shandong Peninsula would become a potential sediment source in winter for shelf sedimentation.

Even though the features of the dynamics and bottom SSC variations has been captured well, only non-cohesive sediments were considered in this model. The median size of sediment distributed along the Shandong Peninsula was 5.5–6.5 Φ (~11–22 μm) (Li et al., 2005), including both non-cohesive and fine-grained sediment. Strong waves could fluidize the cohesive mud bed in the shallow coastal environment, as confirmed by both the laboratory and the model experiments (Maa and Mehta, 1987; Wolanski et al., 1988; Foda et al., 1993; De Wit and Kranenburg, 1997; Sherwood et al., 2018), which can reduce the critical shear stress and produce a highly turbid layer on the seabed. Depending upon the time for consolidation, this bottom sediment may be more easily resuspended during subsequent storm events. To elucidate the effects of wave-current interactions on cohesive mud bed, more data from time-series observation together with numerical approaches are still needed in the future.

6. Conclusions

In this paper, a high-resolution, coupled model of the Bohai and Yellow Seas was used to investigate the contributions of waves and tides to sediment resuspension and transport around Shandong Peninsula, in the Yellow Sea. Two events with strong northerly wind and increased values of SSC were modeled and compared with mooring observations. The second storm event had SSC more than twice that of the first storm event, despite similar significant wave heights. Numerical experiments indicated that the large values of SSC were ascribed to local resuspension, and wave actions played a primary role in the rapid increase of turbidity during the two storm events. Even though the wind direction was different between two storm events, which may affect the wave fetch and propagation, it was not the primary factor that induced the large discrepancy of the bottom SSC between the two storm events. The turbidity difference between the two storm events was mainly ascribed to the changes of wave period by influencing bottom sediment
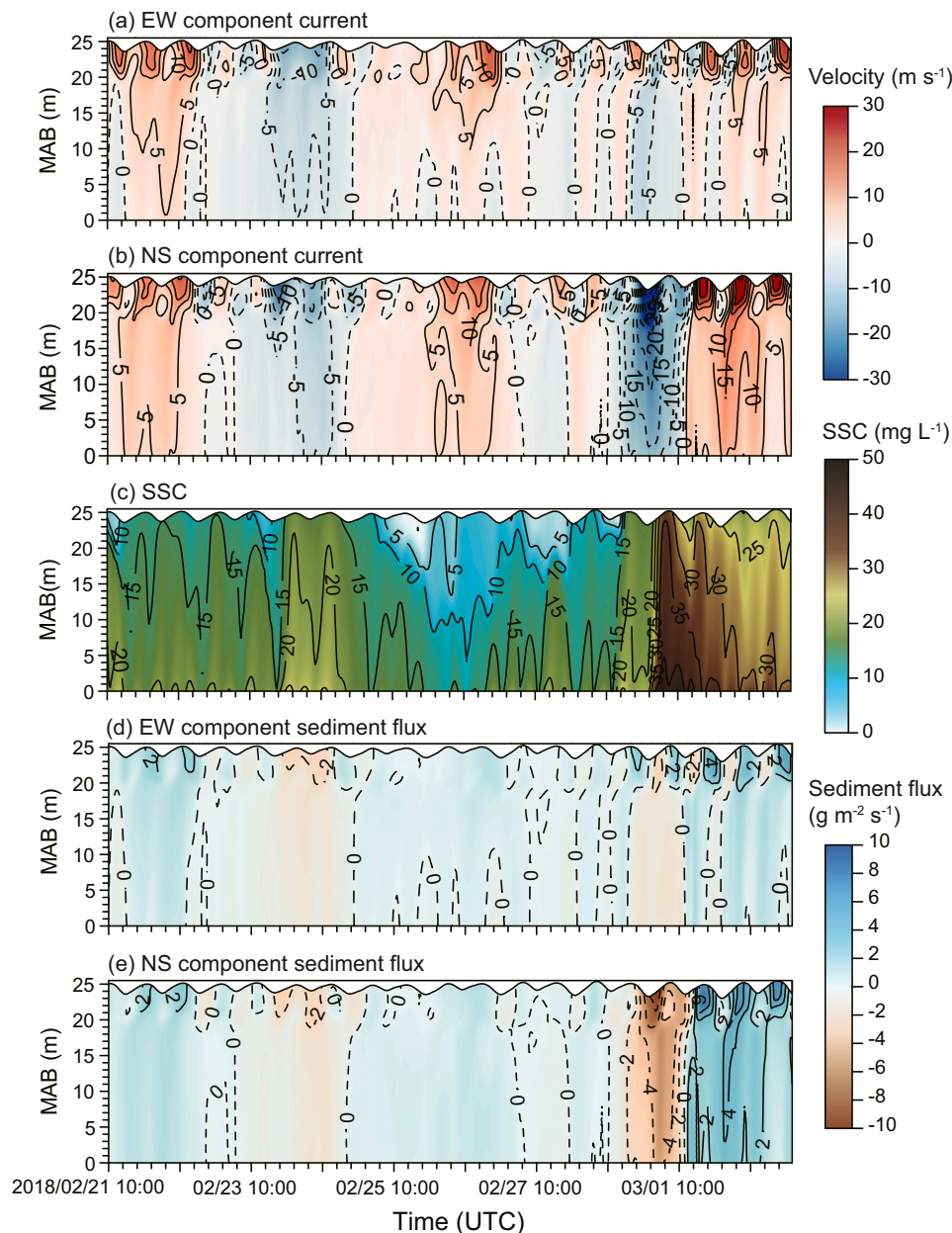
Fig. 13. Time series of vertical distribution of residual currents in east-west component (a) with eastward currents positive, and north-south component (b) with northward currents positive, SSC (c), and sediment flux in east-west component (d) and north-south component (e) in the Control run at station S3.

resuspension. The difference of wave period between the two storm events interpreted 65% of the abnormal increase in wave-induced bottom shear stress during event II, while the remainder was ascribed to the enhancement of nonlinear wave-current interactions. The factor C_{mu} which related to the wave-current-induced bottom shear stress was increased by the increased current velocity when the northerly wind prevailed. Waves induced by northerly winds were mainly responsible for the sediment resuspension to the north and east side of Shandong Peninsula in shallow water in winter. In addition to increasing sediment resuspension, the northerly wind strengthened the residual currents and increased sediment transport southward along the coast of the Shandong Peninsula.

Data availability

In the numerical model, atmospheric forcing data are freely available

from European Center for Medium-Range Weather Forecasts (ECMWF, http://www.ecmwf.int), including dataset of wind, mean sea-level pressure, air temperature, relative humidity, precipitation and net solar shortwave radiation. Initial conditions and two open boundaries (south and east) data are freely obtained from HYCOM (https://www.hycom.org/) and the tidal forcing at the open boundary are derived from the OSU TOPEX/Poseidon Global Inverse Solution (https://www.tpxo.net/). The observed data, including dataset of water level, current, significant wave height, wave period and SSC, in Fig. 2 at station S3 are extracted from Zhao et al. (2019). All the data that support the findings of this study are given in supporting information and are also deposited in Mendeley data set: https://doi.org/10.17632/pc44z8kdvm.1.
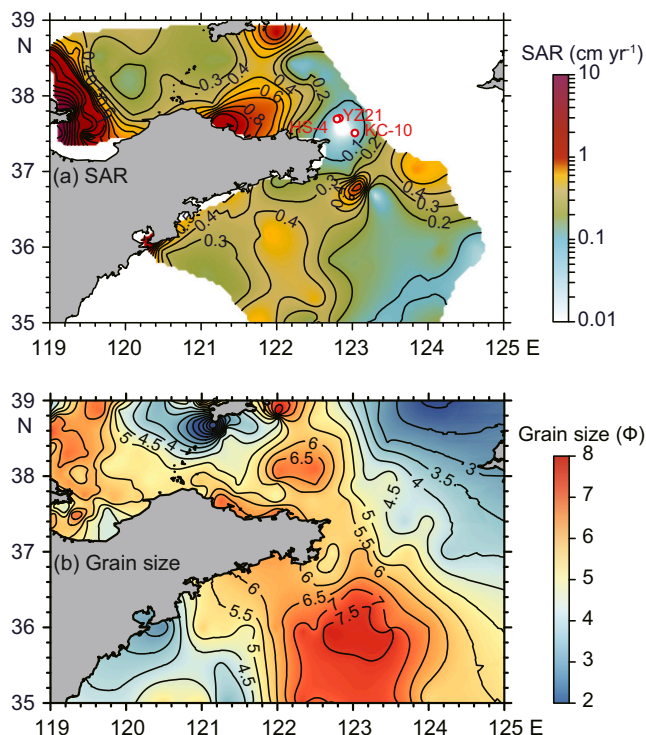
Fig. 14. Horizontal distributions of modern sediment accumulation rate (SAR) derived from the radioisotope (^{210}Pb) measurements (a) and mean grain size (b) of surface sediment (data from Yuan et al., 2020).
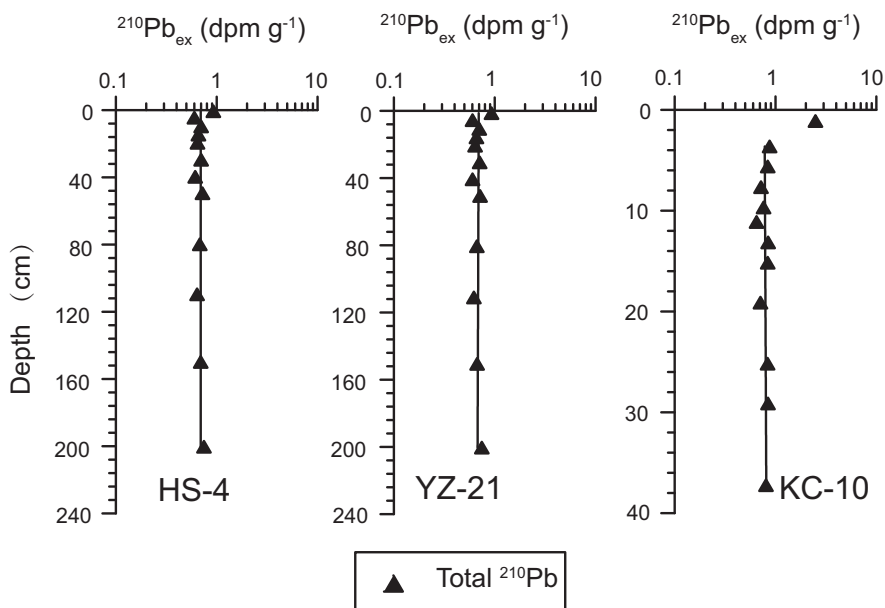
Fig. 15. The ^{210}Pb profiles of cores HS-4, YZ-21, and KC-10 (locations are shown in Fig. 14, data from Li et al., 2002; Zhang et al., 2009; Hu et al., 2011).

Declaration of Competing Interest

The authors declared that they have no conflicts of interest to this work.

Acknowledgments

References

Alexander, C.R., Demaster, D.J., Nittrouer, C.A., 1991. Sediment accumulation in a modern epicontinental-shelf setting: the Yellow Sea. Mar. Geol. 98, 51–72.

Bao, X.W., Gao, G.P., Yan, J., 2001. Three dimensional simulation of tide and tidal current characteristics in the East China Sea. Oceanol. Acta 24, 135–149.

Beardsley, R.C., Limeburner, R., Kim, K., Candela, J., 1992. Lagrangian flow observations in the East China, Yellow and Japan Seas. La mer 30 (3), 297–314.

Bi, N., Yang, Z., Wang, H., Fan, D., Sun, X., Lei, K., 2011. Seasonal variation of suspended-sediment transport through the southern Bohai Strait. Estuar. Coast. Shelf Sci. 93, 239–247.

Bian, C., Jiang, W., Song, D., 2010. Terrigenous transportation to the Okinawa Trough and the influence of typhoons on suspended sediment concentration. Cont. Shelf Res. 30, 1189–1199.

Bian, C., Jiang, W., Greatbatch, R.J., 2013a. An exploratory model study of sediment transport sources and deposits in the Bohai Sea, Yellow Sea, and East China Sea. J. Geophys. Res. Oceans 118, 5908–5923.

Bian, C., Jiang, W., Quan, Q., Wang, T., Greatbatch, R.J., Li, W., 2013b. Distributions of suspended sediment concentration in the Yellow Sea and the East China Sea based on field surveys during the four seasons of 2011. J. Mar. Syst. 121, 24–35.

Blaas, M., Dong, C., Marchesiello, P., Mcwilliams, J.C., Stolzenbach, K.D., 2007. Sediment-transport modeling on Southern Californian shelves: a ROMS case study. Cont. Shelf Res. 27, 832–853.

Booij, N., Ris, R.C., Holthuijsen, L.H., 1999. A third-generation wave model for coastal regions: 1. Model description and validation. J. Geophys. Res. Oceans 104, 7649–7666.

Brand, A., Lacy, J.R., Hsu, K., Hoover, D., Gladding, S., Stacey, M.T., 2010. Wind-enhanced resuspension in the shallow waters of South San Francisco Bay: Mechanisms and potential implications for cohesive sediment transport. J. Geophys. Res. Oceans 115, C11024.

Chen, G., Zhai, F., Li, P., Liu, X., 2016. Numerical study of wave height seasonality in the Yellow Sea. Maine Sci. 40 (11), 155–168.

Choi, B.H., Eum, H.M., Woo, S.B., 2003. A synchronously coupled tide–wave–surge model of the Yellow Sea. Coast. Eng. 47, 381–398.

Chu, P.C., Fralick Jr., C.R., Haeger, S.D., Carron, M.J., 1997. A parametric model for the Yellow Sea thermal variability. J. Geophys. Res. Oceans 102, 10499–10507.

De Wit, P.J., Kranenburg, C., 1997. The Wave-induced Liquefaction of Cohesive Sediment Beds. Estuar. Coast. Shelf Sci. 45, 261–271.

Ding, Y., Bao, X., Yao, Z., Bi, C., Wan, K., Bao, M., Jiang, Z., Song, J., Gao, J., 2019. Observational and model studies of synoptic current fluctuations in the Bohai Strait on the Chinese continental shelf. Ocean Dyn. 69, 323–351.

Dong, L.X., Guan, W.B., Chen, Q., Li, X.H., Liu, X.H., Zeng, X.M., 2011. Sediment transport in the Yellow Sea and East China Sea. Estuar. Coast. Shelf Sci. 93, 248–258.

Egbert, G.D., Erofeeva, S.Y., 2002. Efficient inverse modeling of barotropic ocean tides. J. Atmos. Ocean. Technol. 19 (2), 183–204.

Egbert, G.D., Bennett, A.F., Foreman, M.G.G., 1994. TOPEX/POSEIDON tides estimated using a global inverse model. J. Geophys. Res. Oceans 99, 24821–24852.

Fan, R., Wei, H., Zhao, L., Zhao, W., Jiang, C., Nie, H., 2019. Identify the impacts of waves and tides to coastal suspended sediment concentration based on high-frequency acoustic observations. Mar. Geol. 408, 154–164.

Fang, G., 1986. Tide and Tidal Current Charts for the marginal seas and adjacent to China. Chin. J. Oceanol. Limnol. 4 (1), 1–16.

Foda, M.A., Hunt, J.R., Chou, H.T., 1993. A nonlinear model for the fluidization of marine mud by waves. J. Geophys. Res. Oceans 98, 7039–7047.

Grant, W.D., Madsen, O.S., 1979. Combined wave and current interaction with a rough bottom. J. Geophys. Res. 84, 1797–1808.

Guillou, N., Chapalain, G., 2011. Modelling impact of northerly wind-generated waves on sediments resuspensions in the Dover Strait and adjacent waters. Cont. Shelf Res. 31, 1894–1903.

Harris, C.K., Sherwood, C.R., Signell, R.P., Bever, A.J., Warner, J.C., 2008. Sediment dispersal in the northwestern Adriatic Sea. J. Geophys. Res. Oceans 113, C11S03.

Holligan, P.M., Boois, H.D., 1993. Land Ocean Interactions in the Coastal Zone (LOICZ). Science Plan. Global Change Report (Sweden).

Hsueh, Y., 1988. Recent current observations in the eastern Yellow Sea. J. Geophys. Res. Oceans 93, 6875–6884.

Hu, B., Li, G., Li, J., Yang, M., Wang, L., Bu, R., 2011. Spatial variability of the 210Pb sedimentation rates in the Bohai and Huanghai Seas and its influencing factors. Acta Oceanol. Sin. 33 (6), 125–133 (in Chinese with English abstract).

Hu, Z., Wang, D.-P., He, X., Li, M., Wei, J., Pan, D., Bai, Y., 2017. Episodic surface intrusions in the Yellow Sea during relaxation of northerly winds. J. Geophys. Res. Oceans 122, 6533–6546.

Jacob, R., Larson, J., Ong, E., 2005. M × N communication and parallel interpolation in community climate system model version 3 using the model coupling toolkit. Int. J. High Perform. Comp. Appl. 19, 293–307.

Jiang, W., Pohlmann, T., Sündermann, J., Feng, S., 2000. A modelling study of SPM transport in the Bohai Sea. J. Mar. Syst. 24, 175–200.

Jiang, W., Pohlmann, T., Sun, J., Starke, A., 2004. SPM transport in the Bohai Sea: field experiments and numerical modelling. J. Mar. Syst. 44, 175–188.

Jing, L., Ridd, P.V., 1996. Wave-current bottom shear stresses and sediment resuspension in Cleveland Bay, Australia. Coast. Eng. 29, 169–186.

Komen, G.J., Cavaleri, L., Donelan, M., Hasselmann, K., Hasselmanns, S., Janssen, P., 1994. Dynamics and Modelling of Ocean Waves. Cambridge Univ. Press, p. 532.

Larson, J., Jacob, R., Ong, E., 2005. The model coupling toolkit: a new Fortran90 toolkit for building multiphysics parallel coupled models. Int. J. High Perform. Comp. Appl. 19 (3), 277–292.

Lee, H.J., Chough, S.K., 1989. Sediment distribution, dispersal and budget in the Yellow Sea. Mar. Geol. 87, 195–205.

Li, H., Yuan, Y., 1992. On the formation and maintenance mechanisms of the Cold Water Mass of the Yellow Sea. Chin. J. Oceanol. Limnol. 10 (2), 97–106.

Li, F., Gao, S., Jia, J., Zhao, Y., 2002. Contemporary deposition rates of fine-grained sediment in the Bohai and Yellow Seas. Oceanol. Limnol. Sin. 33 (4), 364–369 (in Chinese with English abstract).

Li, G., Yang, Z., Liu, Y., 2005. Formation Environment of the Seafloor Sediment in the East China Sea. Science Press, Beijing.

Li, G., Wang, H., Liao, H., 2010. Numerical simulation on seasonal transport variations and mechanisms of suspended sediment discharged from the Yellow River to the Bohai Sea. J. Geogr. Sci. 20, 923–937.

Li, G., Li, P., Liu, Y., Qiao, L., Ma, Y., Xu, J., Yang, Z., 2014. Sedimentary system response to the global sea level change in the East China Seas since the last glacial maximum. Earth Sci. Rev. 139, 390–405.

Li, M.Z., Wu, Y., Han, G., Prescott, R.H., Tang, C.C.L., 2017. A modeling study of the impact of major storms on seabed shear stress and sediment transport on the Grand Banks of Newfoundland. J. Geophys. Res. Oceans 122, 4183–4216.

Lie, H.-J., Cho, C.-H., Lee, S., 2009. Tongue-shaped frontal structure and warm water intrusion in the southern Yellow Sea in winter. J. Geophys. Res. Oceans 114, C01003.

Lin, X., Yang, J., 2011. An asymmetric upwind flow, Yellow Sea warm current: 2. Arrested topographic waves in response to the northwesterly wind. J. Geophys. Res. Oceans 116, C04027.

Liu, J.P., Milliman, J.D., Gao, S., 2002. The Shandong mud wedge and post-glacial sediment accumulation in the Yellow Sea. Geo-Mar. Lett. 21 (4), 212–218.

Liu, J.P., Milliman, J.D., Gao, S., Cheng, P., 2004. Holocene development of the Yellow River's subaqueous delta, North Yellow Sea. Mar. Geol. 209, 45–67.

Liu, J.P., Li, A.C., Xu, K.H., Velozzi, D.M., Yang, Z.S., Milliman, J.D., Demaster, D.J., 2006. Sedimentary features of the Yangtze River-derived along-shelf clinoform deposit in the East China Sea. Cont. Shelf Res. 26, 2141–2156.

Liu, J.P., Xu, K.H., Li, A.C., Milliman, J.D., Velozzi, D.M., Xiao, S.B., Yang, Z.S., 2007. Flux and fate of Yangtze River sediment delivered to the East China Sea. Geomorphology 85, 208–224.

Liu, J.P., Xue, Z., Ross, K., Wang, H.J., Yang, Z.S., Li, A.C., Gao, S., 2009. Fate of sediments delivered to the sea by Asian large rivers: long-distance transport and formation of remote alongshore clinothems. Sediment. Rec. 7 (4), 4–9.

Liu, J., Saito, Y., Kong, X., Wang, H., Xiang, L., Wen, C., Nakashima, R., 2010. Sedimentary record of environmental evolution off the Yangtze River estuary, East China Sea, during the last ~13,000 years, with special reference to the influence of the Yellow River on the Yangtze River delta during the last 600 years. Quat. Sci. Rev. 29, 2424–2438.

Luo, Z., Zhu, J., Wu, H., Li, X., 2017. Dynamics of the Sediment Plume over the Yangtze Bank in the Yellow and East China Seas. J. Geophys. Res. Oceans 122, 10073–10090.

Lv, X., Yuan, D., Ma, X., Tao, J., 2014. Wave characteristics analysis in Bohai Sea based on ECMWF wind field. Ocean Eng. 91, 159–171.

Maa, P.Y., Mehta, A.J., 1987. Mud erosion by waves: a laboratory study. Cont. Shelf Res. 7, 1269–1284.

Madsen, O.S., 1994. Spectral wave–current bottom boundary layer flows. In: Coastal Engineering 1994. In: Proceedings of the 24th International Conference on Coastal Engineering Research Council. Kobe, Japan, pp. 384–398.

Martin, J.M., Zhang, J., Shi, M.C., Zhou, Q., 1993. Actual flux of the Huanghe (yellow river) sediment to the Western Pacific Ocean. Neth. J. Sea Res. 31, 243–254.

Miles, T., Glenn, S.M., Schofield, O., 2013. Temporal and spatial variability in fall storm induced sediment resuspension on the Mid-Atlantic Bight. Cont. Shelf Res. 63, S36–S49.

Milliman, J.D., Yun-Shan, Q., Mei-E, R., Saito, Y., 1987. Man's influence on the erosion and transport of sediment by Asian Rivers: the Yellow River (Huanghe) example. J. Geol. 95, 751–762.

Moon, J.-H., Hirose, N., Yoon, J.H., 2009. Comparison of wind and tidal contributions to seasonal circulation of the Yellow Sea. J. Geophys. Res. Oceans 114, C08016.

Naimie, C., Ann Blain, C., Lynch, R.D., 2001. Seasonal mean circulation in the Yellow Sea — a model-generated climatology. Cont. Shelf Res. 21, 667–695.

Nkwinkwa, N., Rouault, M., Johannessen, J.A., 2019. Latent Heat Flux in the Agulhas current. Remote Sens. 11 (13), 1576.

Pang, C., Liang, J., Hu, D., Wang, F., Chen, Y., Bai, H., Bai, X., 2004. Surface circulation patterns observed by drifters in the Yellow Sea in summer of 2001, 2002 and 2003. Chin. J. Oceanol. Limnol. 22, 209–216.

Park, Y.H., 1986. A simple theoretical model for the upwind flow in the southern Yellow Sea. J. Oceanol. Soc. Korea 21 (4), 203–210.

Qiao, L., Zhong, Y., Wang, N., Zhao, K., Huang, L., Wang, Z., 2016. Seasonal transportation and deposition of the suspended sediments in the Bohai Sea and Yellow Sea and the related mechanisms. Ocean Dyn. 66, 751–766.

Qu, L., Lin, X., Hetland, R.D., Guo, J., 2018. The asymmetric continental shelf wave in response to the synoptic wind burst in a semienclosed Double-Shelf Basin. J. Geophys. Res. Oceans 123, 131–148.

Ramesh, R., Chen, Z., Cummins, V., Day, J., D'elia, C., Dennison, B., Forbes, D.L., Glaeser, B., Glaser, M., Glavovic, B., Kremer, H., Lange, M., Larsen, J.N., Le Tissier, M., Newton, A., Pelling, M., Purvaja, R., Wolanski, E., 2015. Land–Ocean interactions in the coastal zone: past, present & future. Anthropocene 12, 85–98.

Riedlinger, S.K., Jacobs, G.A., 2000. Study of the dynamics of wind-driven transports into the Yellow Sea during winter. J. Geophys. Res. Oceans 105, 28695–28708.

Saito, Y., Yang, Z.S., 1994. Historical change of the Huanghe (Yellow River) and its impact on the sediment budget of the East China Sea. In: Proceedings of International Symposium on Global Fluxes of Carbon and its Related Substances in the Coastal Sea-Ocean Atmosphere System, vol. 12. (Japan) Hokkido University, Sapporo, pp. 7–12.

Sanford, L.P., 1994. Wave-forced resuspension of upper Chesapeake Bay muds. Estuaries 17 (1), 148–165.

Schoellhamer, D.H., 1995. Sediment Resuspension Mechanisms in Old Tampa Bay, Florida. Estuar. Coast. Shelf Sci. 40, 603–620.

Shchepetkin, A.F., Mcwilliams, J.C., 2005. The regional oceanic modeling system (ROMS): a split-explicit, free-surface, topography-following-coordinate oceanic model. Ocean Model 9, 347–404.

Sherwood, C.R., Aretxabaleta, A.L., Harris, C.K., Rinehimer, J.P., Verney, R., Ferré, B., 2018. Cohesive and mixed sediment in the regional ocean modeling system (roms v3.6) implemented in the coupled Ocean–Atmosphere–Wave–Sediment Transport Modeling System (COAWST r1234). Geosci. Model Dev. 11 (5), 1849–1871.

Shi, J.Z., Gu, W.J., Wang, D.Z., 2008. Wind wave-forced fine sediment erosion during the slack water periods in Hangzhou Bay, China. Environ. Geol. 55, 629–638.

Signell, R.P., Carniel, S., Cavaleri, L., Chiggiato, J., Doyle, J.D., Pullen, J., Sclavo, M., 2005. Assessment of wind quality for oceanographic modelling in semi-enclosed basins. J. Mar. Syst. 53, 217–233.

Styles, R., Glenn, S.M., 2005. Long-term sediment mobilization at a sandy inner shelf site, LEO-15. J. Geophys. Res. Oceans 110, C04S90.

Su, J., Yuan, Y., 2005. China Offshore Hydrology. China Ocean Press, Beijing (in Chinese).

Swift, D.J.P., Han, G.C., Vincent, C.E., 1986. Fluid processes and sea-floor response on a modern storm-dominated shelf: Middle Atlantic Shelf of North America. Part I: The storm-current regime. In: Knight, R.J., McLean, J.R. (Eds.), Shelf Sands and Sandstones. Canadian Society of Petroleum Geologists, Calgary, Alta, pp. 99–119.

Teague, W.J., Jacobs, G.A., 2000. Current observations on the development of the Yellow Sea warm current. J. Geophys. Res. Oceans 105, 3401–3411.

Teague, W.J., Perkins, H.T., Hallock, Z.R., Jacobs, G.A., 1998. Current and tide observations in the southern Yellow Sea. J. Geophys. Res. Oceans 103, 27783–27793.

Walker, R.G., 1984. Shelf and shallow marine sands. In: Walker, R.G. (Ed.), Facies Models. Geological Association of Canada, Toronto, pp. 141–170.

Wang, X.H., Pinardi, N., 2002. Modeling the dynamics of sediment transport and resuspension in the northern Adriatic Sea. J. Geophys. Res. Oceans 107 (C12), 3225.

Wang, B., Hirose, N., Kang, B., Takayama, K., 2014a. Seasonal migration of the Yellow Sea Bottom Cold Water. J. Geophys. Res. Oceans 119, 4430–4443.

Wang, H., Wang, A., Bi, N., Zeng, X., Xiao, H., 2014b. Seasonal distribution of suspended sediment in the Bohai Sea, China. Cont. Shelf Res. 90, 17–32.

Wang, H., Wu, X., Bi, N., Li, S., Yuan, P., Wang, A., Syvitski, J.P.M., Saito, Y., Yang, Z., Liu, S., Nittrouer, J., 2017. Impacts of the dam-oriented water-sediment regulation scheme on the lower reaches and delta of the Yellow River (Huanghe): a review. Glob. Planet. Chang. 157, 93–113.

Wang, A., Ralston, D.K., Bi, N., Cheng, Z., Wu, X., Wang, H., 2019. Seasonal variation in sediment transport and deposition on a muddy clinoform in the Yellow Sea. Cont. Shelf Res. 179, 37–51.

Wang, C., Liu, Z., Harris, C.K., Wu, X., Wang, H., Bian, C., Bi, N., Duan, H., Xu, J., 2020. The impact of winter storms on sediment transport through a narrow strait, Bohai, China. J. Geophys. Res. Oceans 125, e2020JC016069.

Warner, J.C., Sherwood, C.R., Signell, R.P., Harris, C.K., Arango, H.G., 2008. Development of a three-dimensional, regional, coupled wave, current, and sediment-transport model. Comput. Geosci. 34, 1284–1306.

Warner, J.C., Armstrong, B., He, R., Zambon, J.B., 2010. Development of a coupled Ocean–Atmosphere–Wave–Sediment Transport (COAWST) Modeling System. Ocean Model 35, 230–244.

Wiberg, P.L., Sherwood, C.R., 2008. Calculating wave-generated bottom orbital velocities from surface-wave parameters. Comput. Geosci. 34, 1243–1262.

Wolanski, E., Chappell, J., Ridd, P., Vertessy, R., 1988. Fluidization of mud in estuaries. J. Geophys. Res. Oceans 93, 2351–2361.

Wu, X., Xu, J., Wu, H., Bi, N., Bian, C., Li, P., Wang, A., Duan, H., Wang, H., 2019. Synoptic variations of residual currents in the Huanghe (Yellow River)-derived distal mud patch off the Shandong Peninsula: implications for long-term sediment transport. Mar. Geol. 417, 106014.

Xia, C., Qiao, F., Yang, Y., Ma, J., Yuan, Y., 2006. Three-dimensional structure of the summertime circulation in the Yellow Sea from a wave-tide-circulation coupled model. J. Geophys. Res. Oceans 111, C11S03.

Xiong, J., Wang, X.H., Wang, Y.P., Chen, J., Shi, B., Gao, J., Yang, Y., Yu, Q., Li, M., Yang, L., Gong, X., 2017. Mechanisms of maintaining high suspended sediment concentration over tide-dominated offshore shoals in the southern Yellow Sea. Estuar. Coast. Shelf Sci. 191, 221–233.

Xu, D., Yuan, Y., Liu, Y., 2003. The baroclinic circulation structure of Yellow Sea Cold Water Mass. Sci. China Ser. D Earth Sci. 46 (2), 117–126.

Xu, G., Liu, J., Pei, S., Gao, M., Kong, X., 2016. Transport pathway and depocenter of anthropogenic heavy metals off the Shandong Peninsula, China. Estuar. Coast. Shelf Sci. 180, 168–178.

Yanagi, T., Inoue, K.I., 1995. A numerical experiment on the sedimentation processes in the Yellow Sea and the East China Sea. J. Oceanogr. 51, 537–552.

Yang, Z.S., Liu, J.P., 2007. A unique Yellow River-derived distal subaqueous delta in the Yellow Sea. Mar. Geol. 240, 169–176.

Yu, Q., Wang, Y.P., Flemming, B., Gao, S., 2012. Tide-induced suspended sediment transport: depth-averaged concentrations and horizontal residual fluxes. Cont. Shelf Res. 34, 53–63.

Yuan, Y., Wei, H., Zhao, L., Jiang, W., 2008. Observations of sediment resuspension and settling off the mouth of Jiaozhou Bay, Yellow Sea. Cont. Shelf Res. 28, 2630–2643.

Yuan, P., Wang, H., Wu, X., Bi, N., 2020. Grain-size distribution of surface sediments in the Bohai Sea and the Northern Yellow Sea: sediment supply and hydrodynamics. J. Ocean Univ. China 19, 589–600.

Zang, Z., Xue, Z.G., Bi, N., Yao, Z., Wu, X., Ge, Q., Wang, H., 2017. Seasonal and intra-seasonal variations of suspended-sediment distribution in the Yellow Sea. Cont. Shelf Res. 148, 116–129.

Zeng, X., He, R., Xue, Z., Wang, H., Wang, Y., Yao, Z., Guan, W., Warrillow, J., 2015. River-derived sediment suspension and transport in the Bohai, Yellow, and East China Seas: a preliminary modeling study. Cont. Shelf Res. 111, 112–125.

Zhang, S.W., Wang, Q.Y., Lü, Y., Cui, H., Yuan, Y.L., 2008. Observation of the seasonal evolution of the Yellow Sea Cold Water Mass in 1996–1998. Cont. Shelf Res. 28, 442–457.

Zhang, R., Zhang, G., Huang, B., Zhang, X., 2009. Modern sedimentation rate analysis of the coastal area near the Shandong Peninsula. Mar. Geol. Lett. 25 (9), 15–18 (in Chinese with English abstract).

Zhao, Y., Li, F., Demaster, D.J., Nitrouer, C.A., Milliman, J.D., 1991. Preliminary studies on sedimentation rate and sediment flux of the south Huanghai Sea. Oceanologia et Liminologia Sinica 22 (1), 37–43 (in Chinese with English abstract).

Zhao, G., Bian, C., Xu, J., 2019. A field study of shear stress and suspended sediment concentration in the bottom boundary layer under the influences of tides currents and wind waves. Period. Ocean Univ. China 49 (11), 83–91 (in Chinese with English abstract).

Zong, Y., 2004. Mid-Holocene Sea-level highstand along the Southeast Coast of China. Quat. Int. 117, 55–67.